Structural investigations of chloranilic acid pyrazine cocrystal and ferroelectric 2-methylbenzimidazole

LIU, HUIYU

Structural investigations of chloranilic acid pyrazine cocrystal and ferroelectric 2-methylbenzimidazole

Huiyu Liu

Supervisors Prof. John S.O. Evans and Dr Ivana Evans

Abstract

The purpose of the project was to determine the crystal structures at variable temperatures and investigate the potential structural phase transitions in chloranilic acid pyrazine cocrystal and single-component ferroelectric 2-methylbenzimidazole. The crystal structure of chloranilic acid pyrazine at 120 K was triclinic, P-1, with a=4.7684(2) Å, b=5.8402(3) Å, c=10.6897(5) Å, α=82.038(4)°, β=81.568(4)°, γ=76.938(4)°. It undergoes a phase transition from monoclinic space group C2/m to triclinic space group P-1. We used ideas of rigid bodies and distortion-mode amplitudes to understand what drives the phase transition. The crystal structure of 2-methylbenzimidazole was explored by variable temperature powder and single crystal X-ray diffraction, as well as by variable temperature solid-state NMR and proton spectra calculations. The crystal structure did not change between 120 K and 400 K and was likely to be monoclinic space group Pn.

Acknowledgement

I would like to express my appreciation to all those who provided me the possibility to complete this report. I would first like to give a special gratitude to my supervisors, Prof. John S.O. Evans and Dr Ivana Evans who provided invaluable suggestions and encouragement throughout my research. I would also like to thank Hannah who was involved in the proton spectra calculations for this research and gave me a lot of help. Finally I would like to acknowledge with much appreciation the staff of departmental solid-state NMR service, who conducted the solid-state NMR experiments and gave comments on the spectra.

Content

Chapter 1 Literature review

1.1 Fundamentals of ferroelectricity

A ferroelectric is a polar crystalline material in which an external electric field modulates the spontaneous polarisation.[1-3] Not only does a ferroelectric material possess spontaneous polarisation without the external electric field, but the orientation of its spontaneous polarisation can also be inverted when a reversed electric field is applied.[4] A polarisation-electric field hysteresis loop[5] (Figure 1.1) can be observed by applying an external voltage. At position 1, a saturation polarisation P_{max} that results from orientating all dipoles within a crystal consistent with the direction of a positive electric field is the maximum polarisation that a ferroelectric can possess. If the magnitude of the electric field decreases gradually, the dipoles will point towards the orientation of the external field partially, resulting in the reduction in the polarisation. At position 2, the ferroelectric still retains a remnant polarisation P_R in the absence of an external electric field. A reverse electric field called the coercive field E_c brings the net polarisation to zero. As the negative field increases, the dipoles are reorientated in the direction of the negative field. At position 3, the possession of an equal number of oppositely directed dipole moments leads to the cancellation in net polarisation to zero. At position 4, the polarisation is switched to the opposite direction with the same magnitude as the positive saturation polarisation but a negative sign. It is worth noting that a hysteresis curve might not always be observed, for example, if a material has a large coercive field that cannot complete a closed loop.

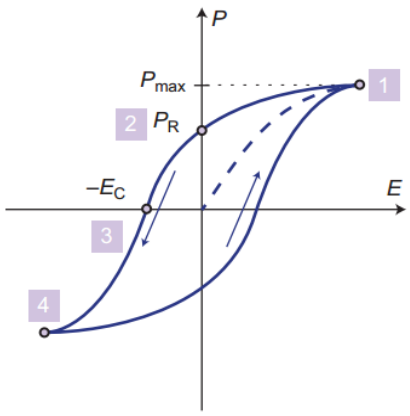

Figure 1.1: The hysteresis loop of polarisation (P) versus electric field (E). [5]

To be ferroelectric, materials always crystallise in a polar space group. Ferroelectricity is often accompanied by a phase transition that can convert a nonpolar centrosymmetric crystal structure to a polar non-centrosymmetric structure. At higher temperature, a material is in a form in which the dipole moments are randomly ordered and cancel out; this is the so-called the paraelectric state.[6] A phase transition may occur at the Curie temperature when reducing the temperature. The material may exhibit ferroelectricity in which case the dipoles within the structure are rearranged without cancelling out each other.[5] Consequently, ferroelectricity in a material may not be achieved at all temperatures.

There are a variety of techniques to examine the potential phase transitions in a material. A critical point, Curie temperature, can be captured by measuring the temperature-dependent dielectric constant ε. A peak anomaly obtained from the permittivity measurement can suggest if a crystal undergoes a structural transformation. The point at which a peak anomaly occurs is the Curie temperature. On the basis of the Curie-Weiss law, the dielectric constant is often described by the equation[7]:

$$\varepsilon = \frac{C}{T - \theta}$$

Where C represents the Curie constant, and the θ is the Curie-Weiss temperature. Phase transitions can be categorised based on the magnitude of the Curie constant C. If C is of the order of 10^3 K, the corresponding ferroelectrics should be triggered by order-disorder phase transition. If the order of C is 10^5 K, the ferroelectrics should show displacive-type phase transition.[4] Moreover, the phase transition can also be either first order or second order, according to whether the derivatives of the chemical potential (μ) of substances vary continuously or discontinuously at the critical point.[8] In a first-order phase transition, the first derivative of μ such as volume (V), entropy (S) and enthalpy (H) changes discontinuously with respect to temperature. In contrast, a phase transition for which the first derivative of μ as a function of temperature is continuous but quantities dependent on its second derivative, e.g. heat capacity (C_p), is discontinuous across the transition temperature is defined as a second-order phase transition. Methods such as differential

scanning calorimetry (DSC) and variable temperature X-ray diffraction (XRD) can be used to detect and characterise a possible structural transformation from a high-temperature non-polar form to a low-temperature polar form, and to determine the order of the phase transition.

1.2 Historical development of organic ferroelectrics

1.2.1 Rochelle salt, the first ferroelectric containing an organic component

Rochelle salt (Figure 1.2), potassium sodium tartrate tetrahydrate ($KNaC_4H_4O_6 \cdot 4H_2O$), by Elie Seignette in 1655.[4] However, it took more than 250 years until Joseph Valasek, who accomplished a systematic study of the dielectric properties and hysteresis characteristics, disclosed the ferroelectric nature of Rochelle salt.[9-11] In 1920, Valasek found that Rochelle salts exhibited a polarisation hysteresis loop (Figure 1.3a) in response to the external electric field.[9] The observation of the electric hysteresis analogous to the ferromagnetic hysteresis marked a milestone in ferroelectric history. Moreover, two years later, the relationship between temperature and the piezoelectric response (Figure 1.3b) was also measured, indicating the existence of a possible phase transition in a Rochelle salt crystal.[10] In the same year, Joseph Valasek coined a term ferroelectricity to designate the behaviours in a Rochelle salt.[11] As a result, a Rochelle salt was reported as the first example of ferroelectric crystal containing organic components. Its crystal structure was first determined by Hughes and Beevers[12] in 1941 by X-ray analysis. More systematical studies[13-16] commented that Rochelle salt exhibits two Curie points (T_{c1}= 255 K and T_{c2}= 297 K). The crystal structures of the two paraelectric phases (below 255 K and above 297 K) belong to the orthorhombic space group $P2_12_12$. Rochelle salt only showed ferroelectricity in a narrow temperature range from 255 K to 297 K. Sandy and Jones[17] suggested an order-disorder type phase transition in Rochelle salt. However, the crystal structure studied in powder X-ray diffraction by Solans et al.[14] did not disclose any evidence for the disorder in the paraelectric state, which is inconsistent with the result published by Sandy and Jones.

The study confirmed that the cystals undergo a second-order phase transition lowering the symmetry of the crystal structure to the monoclinic system (space group $P2_1$). In contrast, a structural reinvestigation by synchrotron X-ray diffraction carried out by Mo and his collaborators[16] indicated that the paraelectric phase at 308 K is disordered, in which potassium atom (K1) occupies two equivalent sites with fraction of 0.5, supporting the theory of order-disorder type ferroelectricty in Rochelle salt (Figure 1.3).

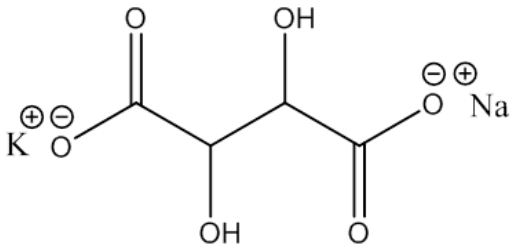

Figure 1.2: Molecular structure of Rochelle salt.

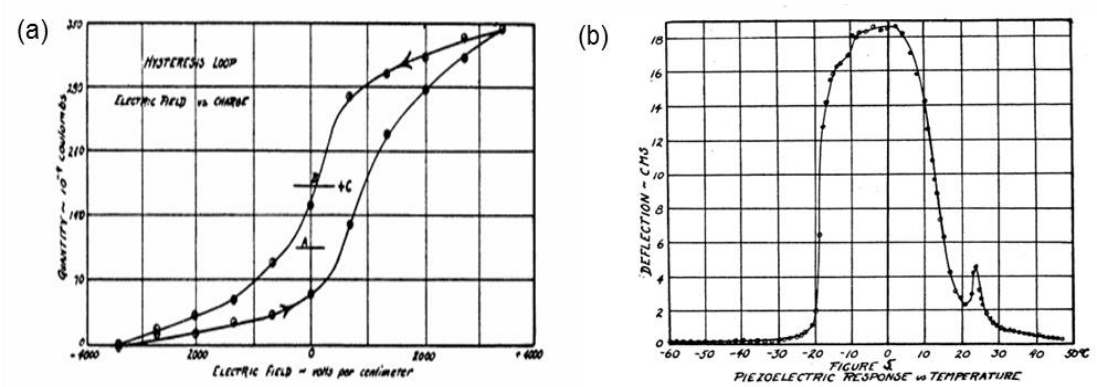

Figure 1.3: (a) Hysteresis loop of the Rochelle salts measured at 273 K; (b) The piezoelectric response of Rochelle salts obtained at various temperatures suggested the existence of phase transition.

1.2.2 KDP, best known hydrogen-bonded organic ferroelectric family

Until 1922, Rochelle salt was the sole known ferroelectric material and scientists showed increasing interests in discovering other materials with ferroelectric characteristics. Busch and Scherer disclosed the ferroelectricity of potassium dihydrogen phosphate (KH_2PO_4) (Figure 1.4), abbreviated as KDP, in 1932.[18]

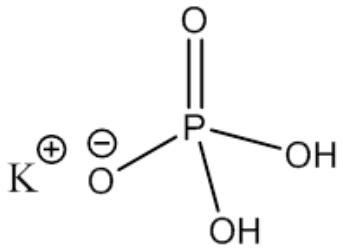

Figure 1.4: The molecular structure of KDP.

KDP is a typical example of a hydrogen-bonded ferroelectric in which phosphate ions, PO_4^{3-}, are bonded into a three-dimensional network through intermolecular hydrogen bonding.[19] The paraelectric state above the Curie point belongs to body-centered tetragonal structure (space group I-42d) which is determined by X-ray diffraction.[20] The two off-center hydrogen bonds, O1-H and O2-H, separated by a distance δ are equivalent (Figure 1.5a). The protons can distribute on both sites with equal probability, forming the disordered non-polarised chains. In 1941, Slater[21] suggested the proton transfer in KDP to be associated with ferroelectricity and published the first substantial molecular theory of ferroelectricity. The relation between ferroelectricity and hydrogen bonds was examined[22] in 2002 and further studied computationally by Koval et al[19] three years later. Koval and collaborators found the evidence for the important roles of hydrogen bonds in triggering the ferroelectricity. The striking isotope effect observed upon deuteration proved the hypothesis proposed by Slater. The deuterated material (DKDP) possesses a significantly higher Curie point (T_c = 229 K) than KDP (T_c=122 K).[22] In ordered ferroelectric phase (space group Fdd2) below the Curie temperature, the hydrogen atoms move collectively towards one of the oxygen atoms and form H-O2 bonds pointing at same orientation. All constituent KDP molecules were connected by hydrogen bonds (O1…H) forming the ordered polarised chains (Figure 1.5b).[23] As a result, the order-disorder type phase transition in a KDP crystal is related to the collective off-centering of protons in the hydrogen bonds.

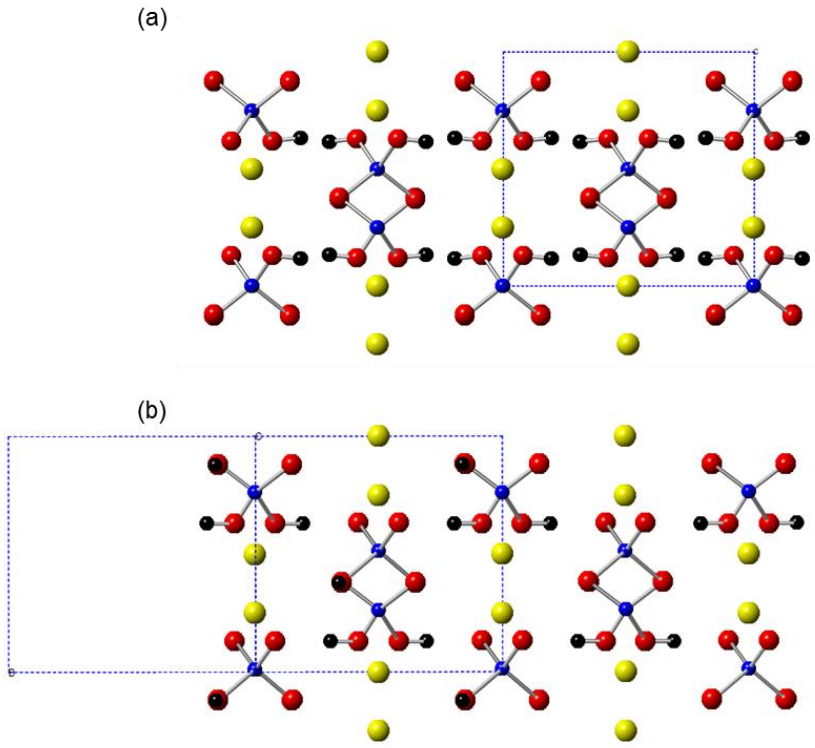

Figure 1.5: The hydrogen-bonding scheme of KDP. (a) The hydrogen bonding of KDP in the disordered paraelectric phase viewed along a-axis.[20] (b)The hydrogen bonding of KDP in the ordered ferroelectric phase viewed along (110). Colour legend: black-H; red-O; blue-P; yellow-K.[23]

1.2.3 Thiourea, the initial report of purely organic ferroelectric of low molecular mass

Although the first-known ferroelectric material contained an organic component, the studies of inorganic ferroelectrics such as barium titanate, $BaTiO_3$, have predominated the field of ferroelectric since 1939.[5] Solomon[24] firstly reported a new purely organic ferroelectric crystal, namely thiourea ($SC(NH_2)_2$) (Figure 1.6), in 1956. He observed that thiourea exhibits hysteresis curve at low temperature and shows a peak anomaly in the dielectric constant. Subsequently, thiourea has been intensively investigated by both experimental and theoretical methods. As in other ferroelectric materials, the ferroelectricity in thiourea is combined with structural phase transitions. From the measured dielectric constant in response to temperature, Goldsmith and White[25] found that a thiourea crystal possesses several types of structures (Figure 1.7 and Table 1.1).

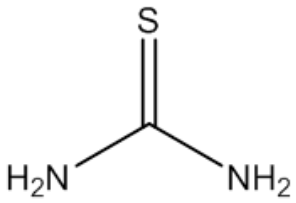

Figure 1.6: The molecular structure of thiourea.

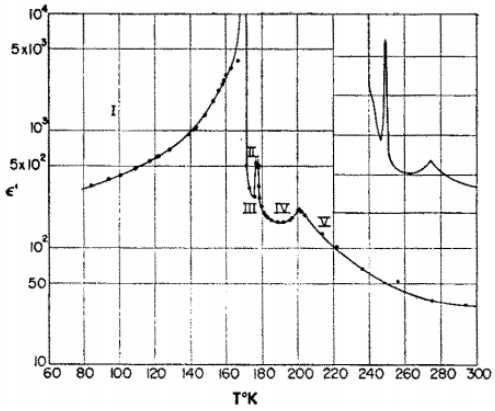

Figure 1.7: The temperature-dependent dielectric constant of thiourea.[25]

Phase	Temperature (K)	Space group	Structure state
Phase Ⅰ	< 169	$P2_1ma$/ $Pb2_1m$	Ferroelectric
Phase Ⅱ	169 - 177	Pbnm	Incommensurate
Phase Ⅲ	177 - 180	Unknow	Ferroelectric
Phase Ⅳ	180 - 202	Unknow	Incommensurate
Phase Ⅴ	> 202	Pnma	Paraelectric

Table 1.1: Summary of the structural information for thiourea.[25-31]

The structure in phase Ⅰ was determined by a neutron diffraction by Elcombe and Taylor in 1968,[27] crystallising in space group $P2_1ma$. A relatively high remanent polarization of 3.0 μC/cm^2 was observed in phase Ⅰ. A phase transition occurs at 169 K converting the lower-temperature ferroelectric phase Ⅰ to the incommensurate phase Ⅱ was affirmed by a significant peak maxima in dielectric measurement at 169 K.[28] The incommensurate structure is orthorhombic (space group Pbnm) studied by single-crystal X-ray diffraction.[29] Another prominent anomalous peak in the dielectric constant occurs at 177 K, which can suggest a phase transition from the incommensurate structure Ⅱ to

another ferroelectric structure Ⅲ. The last phase transition existing at 202 K shows a structural transformation from Phase Ⅳ to the paraelectric phase Ⅴ. The room temperature paraelectric structure which belongs to orthorhombic space group Pnma was investigated using X-ray diffraction.[30]

1.3 Modern organic ferroelectrics

1.3.1 Ferroelectricity in single-component molecular crystals

Croconic acid, $C_5H_2O_5$, that shows high-performance ferroelectricity， is the first example of a single-component organic ferroelectric with above-room-temperature ferroelectricity. A croconic acid molecule contains a five-carbon ring with two hydroxyl groups orienting in the same directions attached to two adjacent carbon atoms (Figure 1.8) and plays a dual role of proton donor and acceptor.[32]

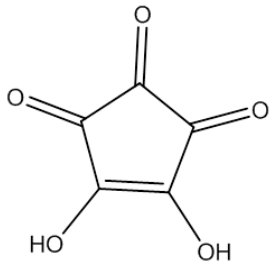

Figure 1.8: The molecular structure of croconic acid.

Recent works[32-37] investigated the structural and ferroelectric properties using X-ray diffraction and density functional theory (DFT). Croconic acid manifested a high spontaneous polarisation up to 21 μC/cm^2. As given in Figure 1.9, the symmetrical rectangular loops in ferroelectric hysteresis measurements at room temperature validated the ferroelectricity in croconic acid.[33] The ferroelectricity is thermally robust up to 380 K, since no maxima were found in the dielectric measurement. A single crystal X-ray diffraction work[37] revealed that croconic acid does not undergo a phase transition to the paraelectric form until it decomposes at 450 K. The structure of croconic acid belongs to orthorhombic space group $Pca2_1$ at room temperature. As depicted in Figure 1.10, all constituent croconic acid molecules are planar and are linked by two crystallographically

independent hydrogen bonds which are labelled as O_1H_1-O_5 and O_2H_2-O_4. One hydrogen bond connects croconic acid molecules, labelled A and B, along the c-axis forming a linear molecular sequence and the other hydrogen bond linking molecule A and D forms a zigzag molecular sequence. In addition, charge transfer (CT), as a consequence of the strong interaction between the electron donating and electron–withdrawing groups along the hydrogen-bonded molecular sequence direction, was revealed to trigger the significant polarisation in croconic acid. The proton transfer between the two croconic acid molecules is responsible for the ferroelectricity.

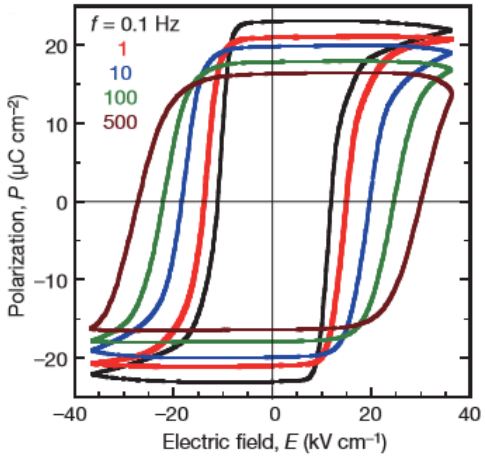

Figure 1.9: Hysteresis loops electric polarisation versus external electric field measured for croconic acid.[33]

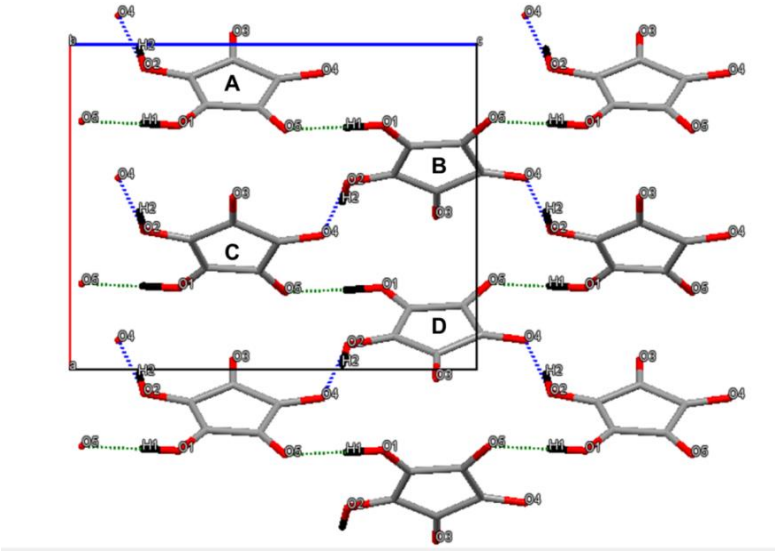

Figure 1.10: Crystal structure of the croconic acid viewed along b-axis in ferroelectric state.[37] The two crystallographically independent hydrogen bonds are represented by blue and green dotted lines respectively.

1.3.2 Ferroelectricity in two-component molecular compounds

Two-component organic ferroelectrics can be classified into two types, based on the different ferroelectric mechanisms: charge-transfer molecular complexes and hydrogen-bonded molecular complexes. Charge-transfer (CT) complexes consist of electron donor (D) and electron acceptor (A) molecules.[1] In a CT complex, the transformation from a neutral state into an ionic state, which is the so-called “neutral-to-ionic (N-I) phase transition”, occurs.[38] A conventional crystalline architecture, namely mixed-stack, shows a propensity to exhibit ferroelectricity forming a face-to-face π-stack with alternating D and A molecules. These mixed-stack crystalline solids are always centrosymmetric because the alternating uncharged D and A molecules are equally spaced apart and are thus paraelectric. Below the Curie temperature, the symmetry breaking caused by CT process occurs yielding a polar non-centrosymmetric structure with a large dielectric constant and spontaneous polarization.[4] The significant interaction between donors and acceptors, which is dependent on the electron donating abilities of the electron-releasing molecules and the electron affinity of the electron-withdrawing molecules, is the result of CT process.[16] Simultaneously, the oppositely charged D and A move towards each other forming dipolar $D^{+}A^{-}$ dimers.[14] By such route, a CT complex can work as a displacive-type ferroelectric transforming the neutral nonpolar D-A-D-A-D-A chain to the polarised DA-DA-DA chain. Although the oppositely charged species displacements and the electronic changes are coupled in the mixed-stack crystals, the ferroelectricity is dominated by intermolecular charge transfer. Tetrathiafulvalene-ρ-chloranil (TTF-CA)[39, 40] and tetrathiafulvalene-ρ-bromanil (TTF-BA)[41, 42] (Figure 1.12) are common examples of mixed-stack charge-transfer organic ferroelectrics.

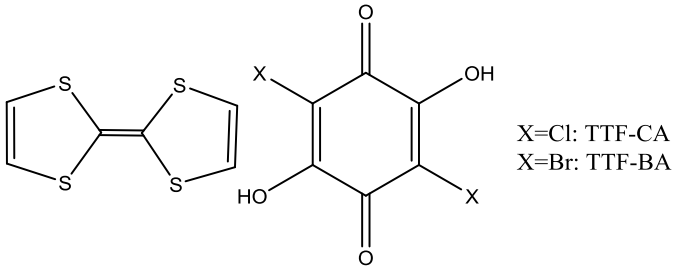

Figure 1.12: The molecular structures of both TTF-CA and TTF-BA.

The study of TTF-CA can been traced back to 1991, when the dielectric constant was measured as a function of temperatures.[40] The neutron scattering and X-ray diffraction experiments were used to determine the structure of both neutral and ionic phases. At room temperature, the neutral structure, which is the nonpolar paraelectric form of a TTF-CA crystal, belongs to a monoclinic system with centrosymmetric space group $P2_1/n$.[43, 44] Below the Curie temperature (81 K), the structural changes are compatible with the electronic changes.[45] The structural distortion can be triggered by a Peierls instability in which the donors and acceptors move relative to one another along the axis of the stack. Also, the first-order N-I phase transition reduces the symmetry of the structure to a polar non-centrosymmetric space group P_n for the ionic ferroelectric state without altering the crystal system.[39, 46] In the crystal, either electron donors or electron acceptors become partially charged as $D^{+\rho}$ and $A^{-\rho}$ where ρ ($0<\rho<1$) is a finite degree of CT. A phase transition was identified by the appearance of a giant peak anomaly in the dielectric constant, which could be induced by either lowering the temperature or applying high pressure (Figure 1.12b).[47] It should be pointed out that the ferroelectric DA-dimerisation results from the valence instability associated with a novel valence transformation. The Peierls instability is responsible for a sharp jump in ionicity (Figure 1.12a)[47] from 0.25-0.3 to 0.65-0.7 at the Curie point. As Torrance[48, 49] reported, an energetic balance between the cost of ionising constituent molecules and gains in the electrostatic energy of the ionised lattice can result in the valence instability. Apart from the temperature- or pressure-dependent dielectric constant, a P-E hysteresis loop (Figure 1.13)[50] provides further evidence for the ferroelectric properties of material.

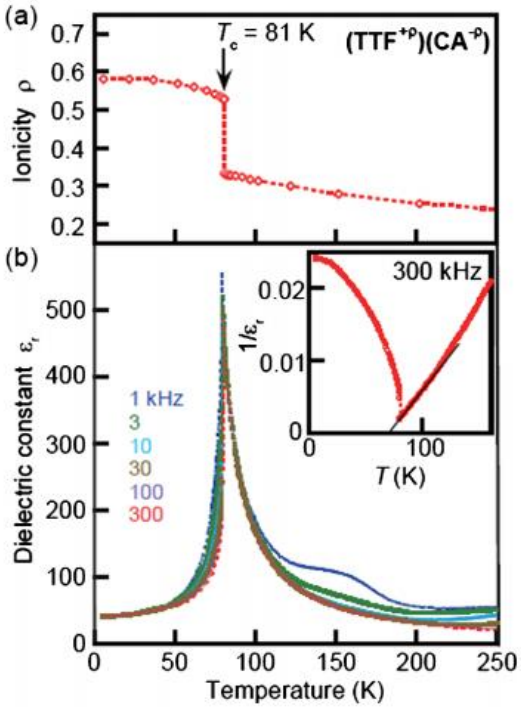

Figure 1.12: (a) Molecular ionicity of TTF-CA varies with temperature and jumps at 81 K. (b) The temperature dependence of dielectric constant in the presence of different frequencies of external electric field.[47]

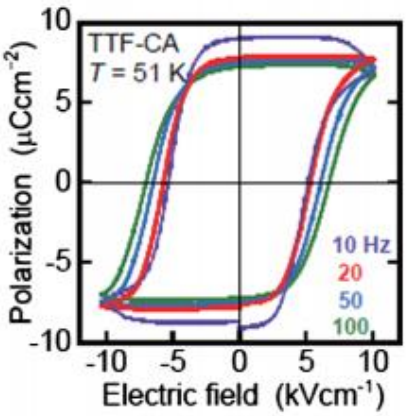

Figure 1.13: Hysteresis loops of TTF-CA with various frequencies at 51 K.[50]

The second type are supramolecular compounds consisting of two different components connected by intermolecular hydrogen bonds, which undergo a distinct displacive phase transition by the proton-transfer mechanism. A well-known group of ferroelectric hydrogen-bonded compounds contain the anilic acid derivatives (H_2xa x=F, Cl, Br, I) as a proton donor (Figure 1.14).

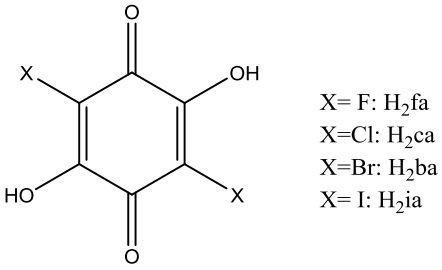

Figure 1.14: The molecular structure of anilic acid

Hydrogen-bonded binary ferroelectric compounds can be classified into two categories in terms of different supramolecular motifs.[51] The first are the simple hydrogen-bonded molecules with linear-chain neutral supramolecular architectures.[52] Hydrogen bonds generate dipoles between the alternating proton donors and proton acceptors arranged in a centrosymmetric fashion, and bind the molecules into nonpolar linear-chains. One of the excellent building blocks that can work as a proton acceptor to produce such molecular ferroelectrics is phenazine ($C_{12}H_8N_2$). The corresponding neutral 1:1 co-crystal (Figure 1.15) consisting of phenazine and anilic acid is abbreviated as Phz-H_2xa ($C_{12}H_8N_2 \cdot C_6H_2X_2O_4$) where X can be F, Cl, Br or I. Figure 1,16 shows the temperature dependence dielectric constant of Phz-H_2xa and Phz-D_2xa.[53] The Curie temperature is 253 K for Phz-H_2ca and 138 K for Phz-H_2ba determined by the temperature-dependent dielectric measurement.[7] At the Curie point, the dielectric constants increase sharply to 1500-2000 and 2500-3000 for Phz-H2ca and Phz-H_2ba respectively.[54] A striking isotropic effect also suggested the significant effect of hydrogens on the ferroelectricity. As shown in Figure 1.17, the proton displacement triggers the ferroelectricity in Phz-H_2xa cocrystals resulting in the proton-donor becoming partially negative whereas the proton-acceptor becomes partially positive. Above the Curie point, the paraelectric structure is monoclinic (space group $P2_1/n$) which is determined by single crystal X-ray diffraction.[53] Below the Curie temperature, the structure of Phz-H_2ca in ferroelectric state belongs to non-centrosymmetric polar space group $P2_1$.[51]

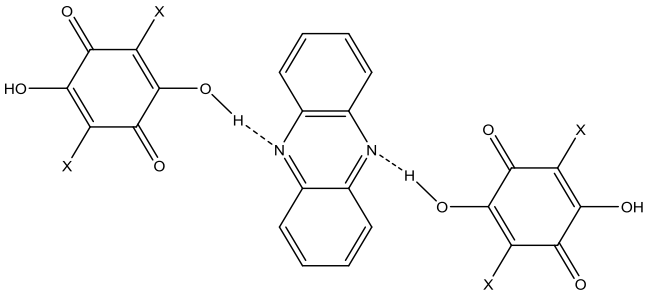

Figure 1.15: Crystal structure of Phz-H_2xa co-crystals.

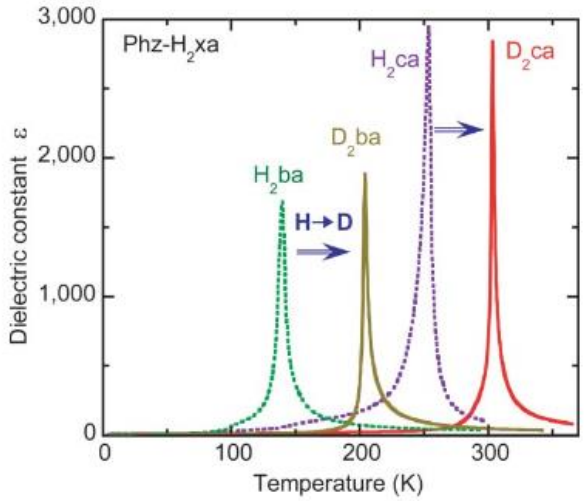

Figure 1.16: The temperature dependence dielectric constant of Phz-H_2xa and Phz-D_2xa (where x= Cl and Br) as a function of temperature. [53]

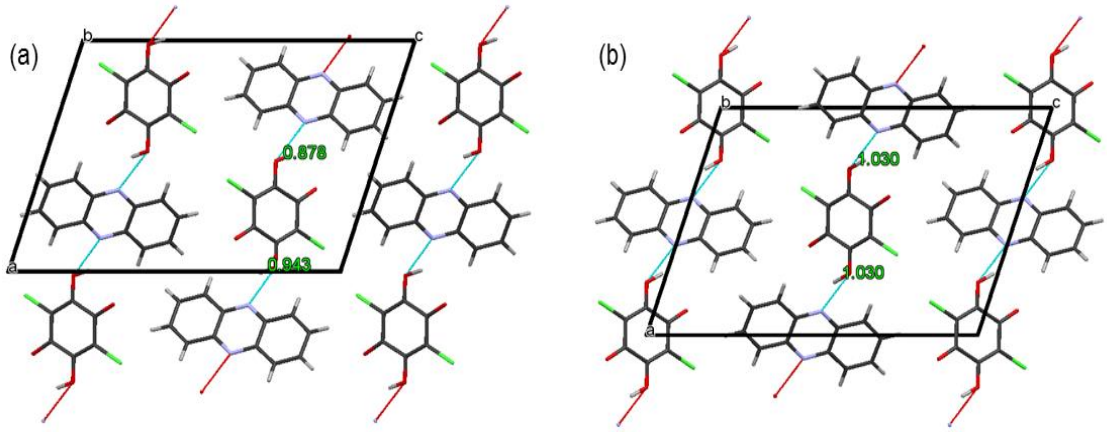

Figure 1.17: Crystal structures of Phz-H_2ca viewed along b-axis. (a) Ferroelectric form of Phz-H_2ca; (b) Paraelectric form of Phz-H_2ca. Colour legend: black-C; grey-H; red-O; blue-N; green-Cl.

The second type of hydrogen-bonded ferroelectrics are linear-chain ionic supramolecules, or salts produced by proton transfer.[55, 56] A recent study[57] has

investigated the ferroelectricity in a series of supramolecular crystals of this kind, also including the anilic acid as proton-donor. The acid-base mechanism yields the ionic supramolecular system, in which stacks are formed by alternating protonated form H-dppz+ and deprotonated form Hxa^- (x= Cl and Br) motifs. [H-dppz][Hca] and [H-dppz][Hba] that are proton-transferred salts, proved to be good organic molecular ferroelectrics.[58] They exhibited large spontaneous polarizations of 2.7 μC/cm^2 and 4.0 μC/cm^2 respectively. The ferroelectric material presented below consists of chloranilic acid (H_2ca) as proton donor group and 2,3-di(2-pyridinyl)pyrazine (dppz) as proton acceptor group (Figure 1.17). P-E hysteresis curves (Figure 1.18a) measured at room temperature, reveals the bistability and electric switchability of spontaneous polarisation validating the ferroelectricity in [Hca][H-dppz] salt.[57] The temperature-dependent dielectric constants were measured along the hydrogen-bonded molecular sequence direction (Figure 1.18b). However, no anomalous peaks in dielectric constant in the temperature range from 0 K to 380 K were observed.[57] The differential scanning calorimetry (DSC) analysis suggested a possible phase transition might occur at 402 K. The phase transition temperature (T_c=402 K) was finally determined by synchrotron X-ray diffraction. Upon cooling, the crystals undergo a structural change transforming the centrosymmetric space group C2/c for the paraelectric form to the Cc space group for the ferroelectric forms.

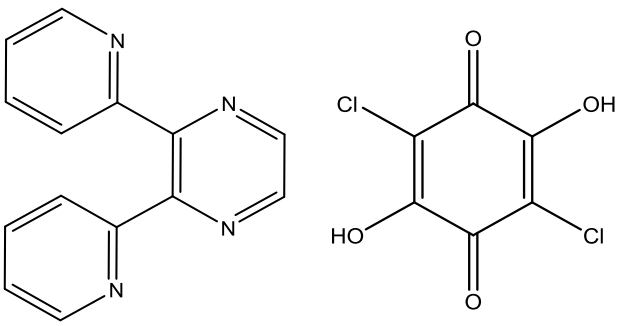

Figure 1.17: The molecular structure of H_2ca-dppz.

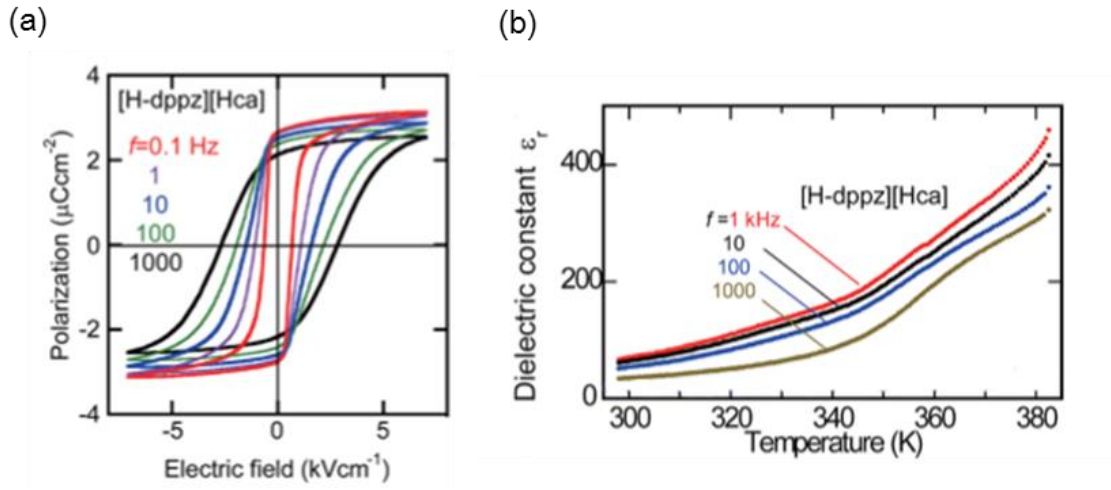

Figure 1.18: (a) P-E hysteresis curve of proton-transferred salts of [H-dppz][Hba] crystals at room temperature. (b) Dielectric constant measured as a function of temperature.[57]

1.4 Aims and objectives of my project

During this project, crystallisation of potential hydrogen-bonded molecular ferroelectric materials was attempted, and a variety of methods such as variable temperature powder X-ray diffraction, variable temperature single crystal diffraction, variable temperature solid-state NMR and thermal analysis were used to examine the structures and possible phase transitions. The structures of the two candidates, chloranilic acid-pyrazine, $C_6H_2O_4Cl_2 \cdot C_4H_4N_2$, abbreviated as CA-Pyz and 2-methylbenzimidazole, $C_8H_8N_2$, abbreviated as 2-MBI, are shown in Figure 1.19. The work is outlined as follows. In chapter 2, the relevant techniques and experimental procedures will be introduced. In the following two chapters, the data analysis and interpretation of the results obtained on CA-Pyz and 2-MBI will be discussed respectively.

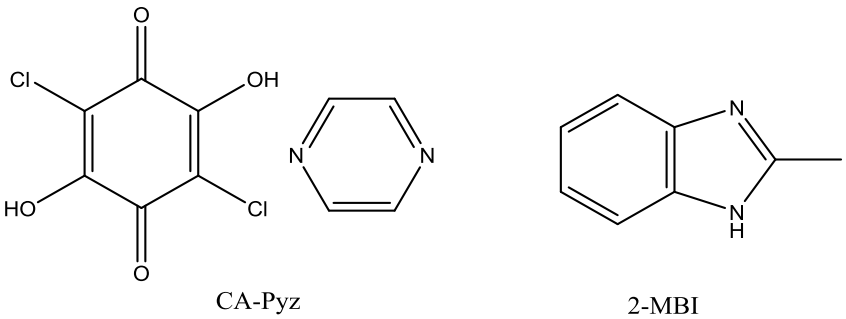

Figure 1.19: The molecular structures of chloranilic acid pyrazine and 2-methylbenzimidazole.

Chapter 2 Experimental section

2.1 Crystal growth

All crystals suitable for single crystal X-ray diffraction were grown using solution methods. Two ways were used to induce crystallisation from solutions. The hot solvent was prepared in order to increase the solubility of the materials. An adequate amount of materials was dissolved in minimal volume of hot solvent to prepare the supersaturated solution. The vials were closed with lids with several small holes pierced, and either left to stand at room temperature or placed in the fridge.

2.2 X-ray diffraction method

2.2.1 Diffraction of X-rays

X-rays are generated when a beam of electrons strike a metal target under the action of high voltage.[59] Copper and molybdenum are commonly used targets to produce X-ray radiation in the laboratory. The diffraction of X-ray by a crystal was initially disclosed by Max von Laue in 1912.[60] Diffraction refers to an interference phenomenon when a wave encounters obstacles or slits. If a crystal is regarded as consisting of periodically repeating planes, each set of the parallel planes (Figure 2.1), characterised by an interplanar spacing d_{hkl}, can diffract X-ray radiation.[61] When the Bragg condition, given in Equation 2.1, is fulfilled, the reflections of X-rays by a crystal are observed because adjacent reflected beams interfere constructively.[62]

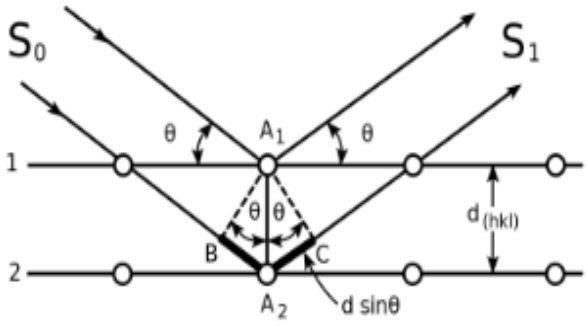

Figure 2.1: Bragg reflection from a set of crystal planes with a spacing d_{hkl}.[61] .

$$n\lambda = 2d_{hkl}sin\theta$$ Equation 2.1

Based on the Bragg's Law, the interplanar spacing between each set of Miller (hkl) planes is related to the angle of reflection, the relationship of d_{hkl} to unit cell dimensions a, b and c is defined as follows[60]:

For monoclinic system $\frac{1}{d^2} = \frac{1}{sin\beta^2}(\frac{h^2}{a^2} + \frac{k^2 sin\beta^2}{b^2} + \frac{l^2}{c^2} - \frac{2hlcos\beta}{ac})$

For orthorhombic system $\frac{1}{d^2} = \frac{h^2}{a^2} + \frac{k^2}{b^2} + \frac{l^2}{c^2}$

For individual hkl reflection, the intensity I_{hkl} of X-ray scattered can be calculated if the structure is known. Equation 2.2 is used to work out the intensity of a reflection.[63]

$$I_{hkl} = cL(2\theta)P(2\theta)A(2\theta)j_{hkl}|F_{hkl}|^2$$ Equation 2.2

where c, L, P and A are the scale, Lorentz, polarisation and absorption factors respectively; j is the multiplicity which stands for the number of symmetry equivalents.

X-rays are scattered elastically by the electrons in an atom. The atomic scattering factor, f, is the term which describes the effectiveness of an atom scattering an incident beam, or its scattering power. In order to estimate the total scattering from a crystal, the scattering from all individual atoms in the unit cell are added together, resulting in a quantity called structure factor F_{hkl}. The structure factor, F_{hkl}, is dependent on the atomic positions (expressed as fractional atomic coordinates (x_n, y_n, z_n) and scattering factor of each atom (f_n) as shown by Equation 2.3:[64]

$$F_{hkl} = \sum_n f_n e^{2\pi i(hx_n + ky_n + lz_n)}$$ Equation 2.3

2.2.2 Single crystal X-ray diffraction

Single crystal X-ray diffraction is the primary method for crystal structure determination. It can provide accurate information about unit cell parameters, space group and the precise atomic positions, and therefore bond lengths and bond angles. The intensity of a hkl reflection is measured individually, and it is proportional to the square of the modulus of the structure factor. Mathematically, the magnitude of the structure factor can be calculated if the intensity of a reflection is measured; however, the phase information is

lost in the experiment. The electron density can be derived based on Equation 2.4 if the structure factors are known.[65]

$$\rho(x,y,z) = \frac{1}{V}\sum_h \sum_k \sum_l F_{hkl}\, e^{-2\pi i(hx+ky+lz)} \qquad \text{Equation 2.4}$$

To solve the phase problem, an SIR92[66] structure solution software was used within the CRYSTALS[67] software. All atoms apart from hydrogens were refined anisotropically. Hydrogens were located using difference Fourier maps and refined with isotropic temperature factors. The positions of hydrogens were refined freely by introducing a bond length restraint. Three parameters Chebyshev weighting scheme[68] was then applied to enhance the precision of the refinement.

2.2.3 Powder x-ray diffraction

Powder X-ray diffraction (PXRD) is a rapid analytical technique that is used routinely for phase identification and purity assessment of the materials.[63] However, it also provides precise information on unit cell parameters and their temperature dependence, which can reveal phase transitions and the structural changes in a system. Ideally, in a powder diffraction experiment, the crystallites should be orientated randomly in all directions. However, preferred orientation can induce severe problems.[69] The correctness of the intensity of reflections can be influenced by this strong tendency for the crystallites to arrange in a particular direction. Problems related to preferred orientation can be overcome by collecting data in capillary mode or by applying a preferred orientation correction (March-Dollase or Spherical harmonic).

2.3 Powder diffraction patterns analysis methods

Powder diffraction data were analysed by the Rietveld[70] method using TOPAS Academic[71] software. Rietveld refinement was used to refine crystal structures by fitting calculated powder patterns to the experimental powder patterns. The Rietveld method is a structure refinement process in which powder diffraction patterns are fitted with a number of parameters (both structure model parameters for a structure and instrumental

parameters). It is based on non-linear least-squares fitting process which is carried out until the minimised quantity of residual S_y, which is determined by Equation 2.5.[72]

$$S_y = \sum_i W_i(y_i - y_{ci})^2 \quad \text{Equation 2.5}$$

S_y is the weighted difference between the experimental pattern and the simulated pattern in terms of peak intensity at each i^{th} step; W_i (equal to the reciprocal of y_i) is the weighting, y_i is the observed intensity at each step and y_{ci} is the calculated intensity at each step. The calculated intensity y_{ci}, given in Equation 2.6, is obtained by a summation of the calculated contributions from adjacent reflections and the background. [69]

$$y_{ci} = s\sum_K L_K|\mathrm{F}_K|^2\Phi\,(2\theta_i - 2\theta_K)P_K A + y_{bi} \quad \text{Equation 2.6}$$

S is scale factor; K represents the Miller indices hkl for a Bragg reflection; L_k includes the Lorentz, polarisation and multiplicity factors; Φ is the reflection profile function. It is determined from the value of structure factor F_{hkl}, which contains the information about atom types and atomic positions in the structure. In other words, the structure model is refinable in a Rietveld refinement.

In order to judge whether the best fit is attained, several criteria of fit are introduced. The R-weighted pattern, R_{wp}, and the statistically expected R value, R_{exp}, are defined in the Equation 2.7 and Equation 2.8, respectively. [73]

$$R_{wp} = \sqrt{\frac{\sum w_i(y_i - y_{ci})^2}{\sum w_i(y_i)^2}} \quad \text{Equation 2.7}$$

$$R_{exp} = \sqrt{\frac{(N-P)}{\sum W_i(y^i)^2}} \quad \text{Equation 2.8}$$

In Equation 2.5, N represents the number of observations while P is the number of parameters.

The goodness-of-fit (GOOF, χ) is given in Equation 2.9 which reflects the quality of a refinement.[73] The R_{exp} should approach the same value as R_{wp}. That is, a GOOF value of 1 should ideally be obtained.

$$GOOF = \sqrt{\chi^2} = \frac{R_{wp}}{R_{exp}} \quad \text{Equation 2.9}$$

2.4 Solid-state nuclear magnetic resonance (SSNMR)

Solid-state NMR was also used as a complementary method for identification of phase transitions. NMR describes the phenomenon which is related to the behavior of nuclei of atoms. When a charge is spinning, it can produce a magnetic field.[74] In the presence of applied magnetic field, the nuclei of atoms possess two spin states. One state has low spin energy whose direction is consistent with the external magnetic field while another state exhibit high energy whose orientation is opposite to the external magnetic field. The difference in populations of higher and lower energy spin states give rise to the NMR signals. Normally, dipolar interaction and anisotropic interaction in solids cannot be eliminated due to the lack of molecular motions. The effects of anisotropic interactions result in the presence of broad lineshapes in the spectra. When a material undergoes a structural transformation, the symmetry is broken which can cause changes in the environments of protons or carbon atoms in the molecule. As a result, the variation in the ^{13}C or ^{1}H spectra of the same material may suggest a phase transition in the sample. Solid-state NMR spectra presented here were collected by the Departmental solid stat NMR service.

Chapter 3 Structure determination of chloranilic acid pyrazine

3.1 Introduction

Hydrogen-bonded organic materials are one of the important categories of molecular ferroelectrics. Anilic acid has been extensively studied[75] for its ability to produce two-component hydrogen-bonded organic ferroelectrics. Anilic acid abbreviated as H_2xa acts as a strong proton donor group. As shown in Figure 3.1, H_2xa ($C_6H_2X_2O_4$) undergoes a series of deprotonation processes with pK1=0.73 and pK2=3.08 and can form various hydrogen bonding types (Figure 3.2) in combination with bases such as tetrathiafulvalene(TTF), 2,3-di(2-pyridinyl)pyrazine(dppz) and phenazine (Phz).

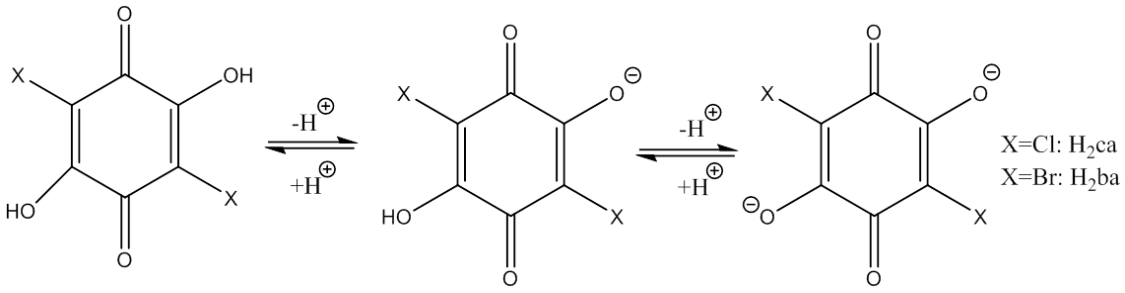

Figure 3.1: Deprotonation and protonation process of anilic acid.

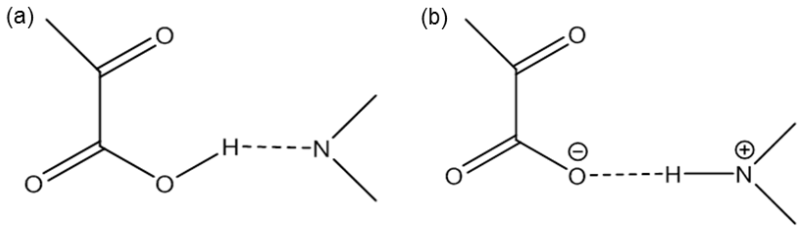

Figure 3.2: Hydrogen-bonding interaction formed between the proton donor group and the proton acceptor group. (a) Hydrogen-bonding in neutral form. (b) Hydrogen-bonding in ionic form.

Another novel characteristic is that anilic acid contains β-diketone enol units (HO-C=C-C=O) which can yield strong intra- or intermolecular hydrogen-bonding interactions, the so-called resonance-assisted hydrogen bonding (RAHB), through keto-enol tautomerisation (Figure 3.3).[1] The hydrogen-bonding interactions play an important role in the phase transitions between FE and PE forms because they are highly directional. Movements of the proton between the proton donor atom and the proton acceptor atom

are often responsible for the polarization reversal. As mentioned in section 1.2, TTF-H_2ca and TTF-H_2ba are prototypical hydrogen-bonded multi-component organic ferroelectrics containing an anilic acid component.[40, 41]

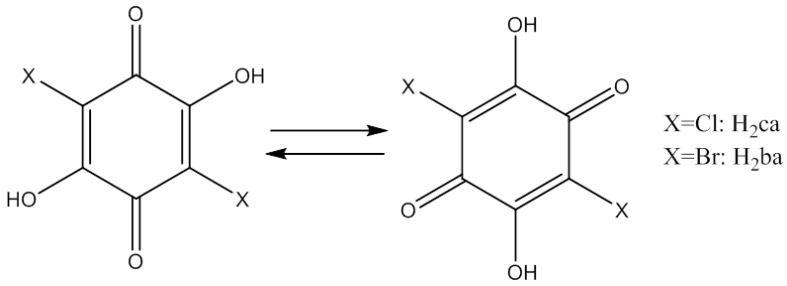

Figure 3.3: Proton tautomerism of chloranilic acid-pyrazine where X=Cl and Br.

Chloranilic acid can combine with pyrazine in a 1:1 or 1:2 ratio. The structure of both neutral form and ionic form chloranilic acid-pyrazine complex were investigated. In 1999, Ishida and Kashino[76] investigated the two-dimensional hydrogen-bond network of neutral 1:1 chloranilic acid pyrazine (CA-Pyz) cocrystals based on IR data. They reported that the crystal structure of CA-Pyz belongs to monoclinic C2/m space group at room temperature. The two components are linked by hydrogen bond forming a one-dimensional chain. The space group, possessing 2/m symmetry, is centrosymmetric and nonpolar.[77] No acid-base interaction involving a proton transfer is observed. So far, the low-temperature structure of CA-Pyz has not been reported. If CA-Pyz exhibits ferroelectricity at low temperature, it would have to undergo a phase transition to a non-centrosymmetric space group.

The aim of this work was to determine the low-temperature structure of CA-Pyz and investigate whether CA-Pyz undergoes a structural phase transition to a potentially ferroelectric noncentrosymmetric structure. Herein, the 120 K and 290 K crystal structures of CA-Pyz are determined from single crystal X-ray diffraction and the phase transition identified investigated by powder X-ray diffraction. The best model to fit all data was attempted in Topas Academic. We have used a variety of approaches for understanding and interpreting the powder data including the use of rigid bodies and the first report of applying “molecular distortion modes” to describe the phase transition of a

molecular system.

3.2 Experimental section

3.2.1 Sample preparation

Single crystals of CA-Pyz were obtained from the slow evaporation of acetonitrile solution with chloranilic acid (Aldrich) and pyrazine (Aldrich, 99%) in a 1:1 molar ratio. Chloranilic acid (0.0627g, 0.3mmol) and pyrazine (0.0240g, 0.3 mmol) were dissolved in minimal volume of acetonitrile respectively with gentle heating for 30 minutes. Then, the solutions were combined in 10 mL sample phials. Four phials of samples were prepared. Two of them were left to crystallise at room temperature while others were permitted to grow crystals in the fridge. Red crystals appeared after one week in phials which were in the fridge. Two days later, red crystals also appeared at room temperature. These crystals were finely ground into powder and used for both room temperature and variable temperature powder X-ray diffractions.

3.2.2 Single crystal X-ray diffraction

An Oxford Gemini S Ultra diffractometer with a CCD detector was used to collect data at 120 K and 290 K using Mo Kα radiation (λ=0.71073 Å). The exposure time used was 15 seconds per frame. A Cryostream Plus Controller was used to control the experimental temperature. Both crystal structures were solved by a default SIR92[66] structure solution run the CRYSTALS[67] software. All atoms apart from hydrogens were refined anisotropically. The hydrogen atoms were located by difference Fourier maps and refined isotropically with an O-H bond length restraint. A three parameter Chebyshev weighting scheme was also applied. The crystal was rhombus-shaped under the polarised microscope.

3.2.3 Powder X-ray diffraction

For investigating the phase transition, both flat plate and capillary PXRD experiments were carried out. Ground crystals were sifted through a 120 mesh sieve and randomly sprinkled onto the silicon flat plate which was covered with a thin layer of Vaseline. Then, the plate was placed into a Bruker D8 ADVANCE diffractometer (d9) equipped with 6 mm variable divergence slit (v6) and Lynx-Eye detector. An Oxford Cryosystems PheniX was used to control the temperature during the measurement. It was used to cool the sample from 310 K to 12 K and then to warm from 12 K back to 310 K ramping at 15 K per hour. The powder patterns were recorded at 63 temperatures over a 2θ range of 5°-50° using a step size of 0.02°. Each data collection took 20 minutes which means every collection experienced a 5 K changed in temperature. A Bruker D8 diffractometer equipped with a Mo tube (d6) was used to repeat the variable temperature measurement of CA-Pyz. A 0.3 mm borosilicate glass capillary instead of a flat plate was used to hold the sample. The capillary was filled to a length of 30 mm by gently tapping small amounts of sample down the tube. The capillary was flame-sealed and then held in a 1 mm internal-diameter 5 mm external-diameter 20 mm-length capillary tube using superglue and attached to the goniometer head. The Cryopad control software was used to control a Oxford Cryosystems Cryostream, and set the experimental temperature. 50 data sets were recorded from 1°-30° using a step size 0.01°. Several different data collections were performed as the sample was cooled and warmed at different rates. However, all samples showed similar behavior. In order to collect better data, a 0.7 mm borosilicate glass capillary was used. 65 data sets were collected on cooling from 1°-30° using a step size 0.01° on the “d6”. Each data set took 55 minutes and experienced a 4 K change in temperature.

3.3 Results and discussion

3.3.1 Crystal structures

A two-temperature single crystal X-ray diffraction study at 120 K and 290 K suggested that a phase transition occurs in this material. These two data sets (see Table 3.1) were

collected from different crystals.

	120 K	290 K
Chemical formula	$C_{10}H_6N_2O_4Cl_2$	$C_{10}H_6N_2O_4Cl_2$
Mr	289.07	289.07
Crystal system	Triclinic	Monoclinic
Space group	P-1	C2/m
Z	1	2
a (Å)	4.7684 (2)	8.3037 (5)
b (Å)	5.8402 (3)	6.6683 (2)
c (Å)	10.6897 (5)	10.9762 (2)
α (º)	82.038 (4)	90
β (º)	81.568 (4)	101.60 (3)
γ (º)	76.938 (4)	90
Volume (Å³)	285.134 (12)	594.44 (11)
No. of measured reflections	10424	3353
No. of observed reflections	1874	482
No. of parameters	85	54
R, Rw （%）	7.127, 9.733	5.878, 8.757
I/Sigma cutoff	2	2

Table 3.1 Crystallographic data of chloranilic acid pyrazine at 120 K and 290 K.

The RT phase of CA-Py crystallised in the centrosymmetric space group C2/m, which is consistent with the result reported by Ishida and Kashino. Figure 3.4 shows the crystal structure obtained at 290 K. Alternating chloranilic acid and pyrazine molecules are linked by intermolecular hydrogen bond forming a hydrogen-bonded chain. The chloranilic acid and pyrazine molecular planes are twisted with respect to each other. The layers of hydrogen-bonded CA-Pyz stack along crystallographic b-axis without remarkable intermolecular interactions forming the three-dimensional crystal structure

(Figure 3.4). The LT phase of CA-Pyz is first reported herein. The LT structure, shown in Figure 3.5, belongs to triclinic space group $P\bar{1}$ which is still centrosymmetric. In this structure, chloranilic acid and pyrazine molecules show the same connectivity as RT phase. Although the structure of CA-Pyz exhibited significant changes, it did not transfer to a ferroelectric non-centrosymmetric phase. That is, CA-Pyz does not exhibit ferroelectricity at a lower temperature.

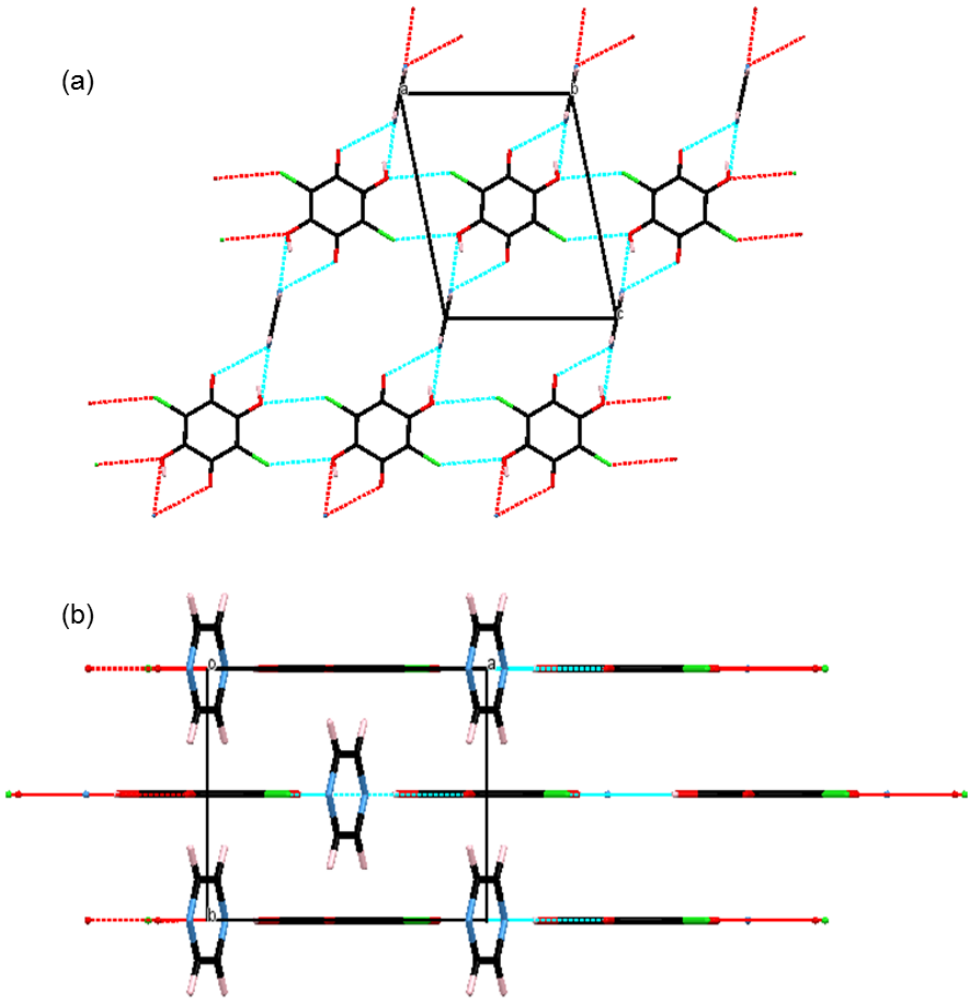

Figure 3.4: Crystal structures of CA-Pyz obtained at 290 K from single crystal X-ray diffraction viewed along (a) stacking b-axis and (b) crystallographic a-axis. Colour legend: black-C; pink-H; blue-N; red-O; green-Cl. The hydrogen bonds are indicated by turquoise dotted lines.

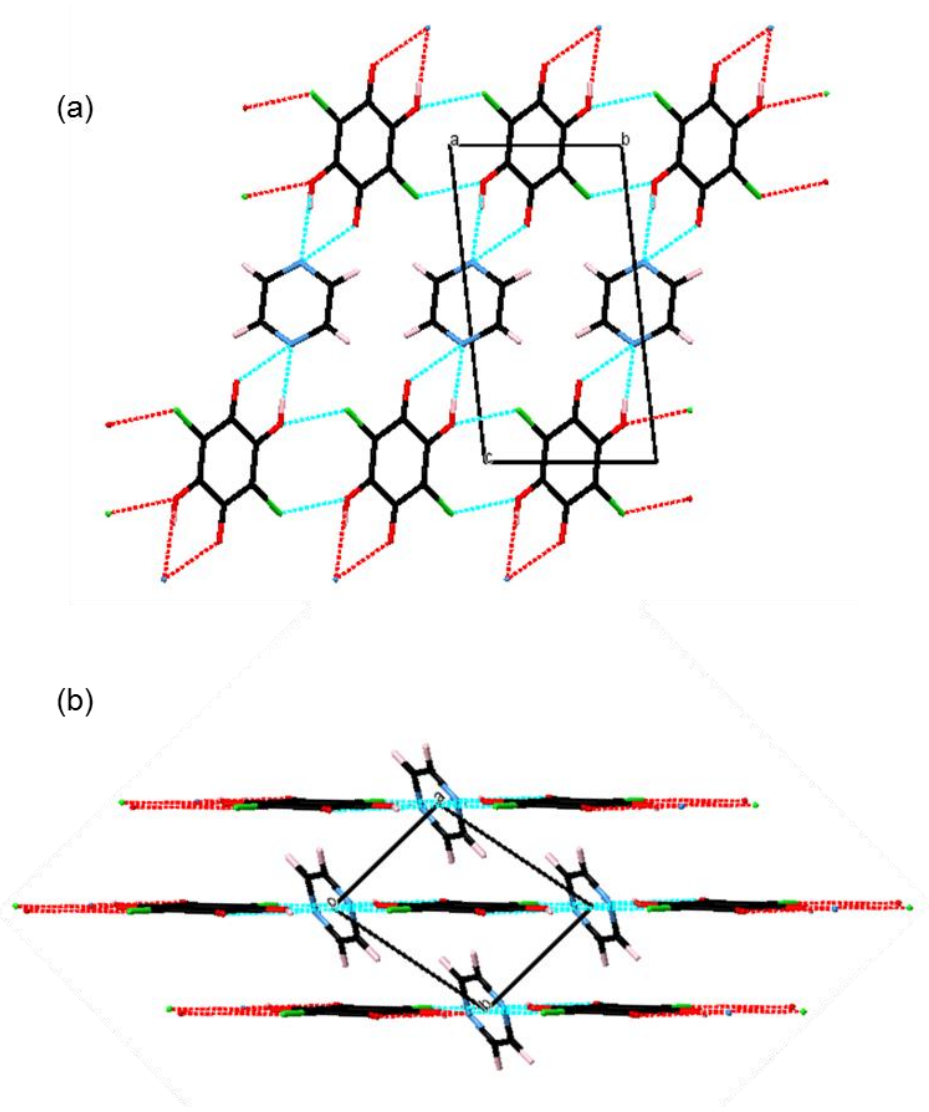

Figure 3.5: Crystal structures of CA-Pyz obtained at 120 K from single crystal X-ray diffraction viewed along (a) crystallographic a-axis and (b) crystallographic c-axis. Colour legend: black-C; pink-H; blue-N; red-O; green-Cl. The hydrogen bonds are indicated by turquoise dotted lines.

3.3.2 Variable temperature powder X-ray diffraction (PXRD)

Although CA-Pyz did not undergo a ferroelectric-type structural change, the questions of how the two structures relate to each other, as well as what drives the phase transition, still remain. One way to understand this is to consider the RT structure as the “parent” and the LT structure as the distorted “child” structure. A transformation matrix (Matrix 3.1) was worked out in ISODISTORT[78] which converts the HT parent structure (Figure 3.6a) to the LT child structure (Figure 3.6b). This matrix shows how the cells of the two structures are related. It also shows how we can potentially analyse variable temperature

powder data using a single structural model based on the P-1 cell. Here, we would expect the unit cell parameters a and b and the unit cell angles alpha and beta to become equal at the phase transition (see Table 3.2).

$$M = \begin{pmatrix} 1/2 & 1/2 & 0 \\ 1/2 & -1/2 & 0 \\ 0 & 0 & -1 \end{pmatrix}$$ Matrix 3.1

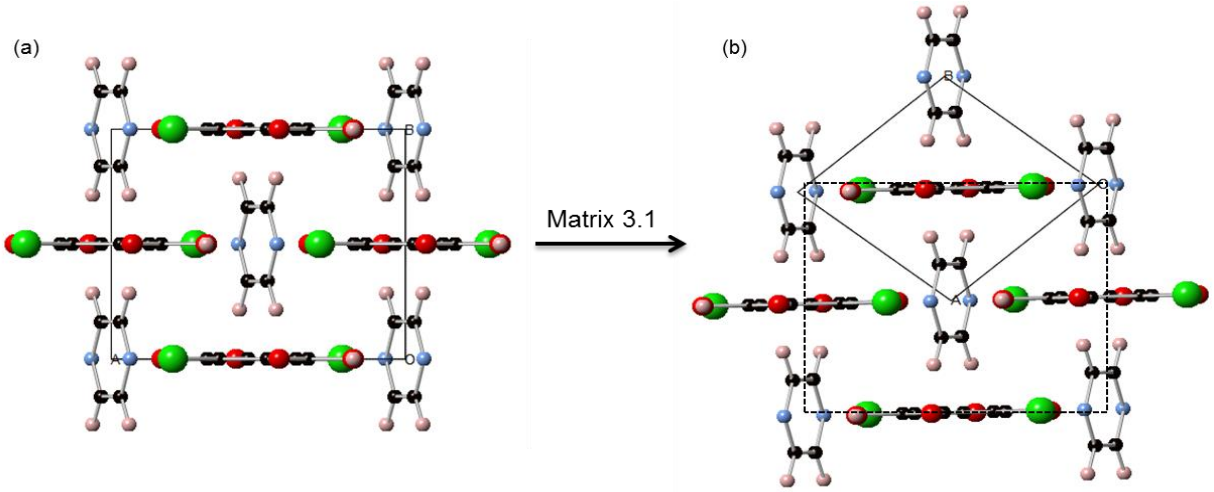

Figure 3.6: The crystal structures of (a) RT parent and (b) LT child viewed down c-axis. The dotted square shown in (b) indicates the unit cell of RT parent.

	HT "parent" cell	LT "child" cell	LT cell
space group	C2/m	$P\bar{1}$	$P\bar{1}$
a (Å)	8.3037 (5)	5.3174	4.7684 (2)
b (Å)	6.6683 (2)	5.3174	5.8402 (3)
c (Å)	10.9762 (2)	10.9930	10.6897 (5)
α (º)	90	80.97	82.04 (4)
β (º)	101.60 (3)	80.97	81.57 (4)
γ (º)	90	77.46	76.94 (4)

Table 3.2: Unit cell of HT "parent" structure determined by powder X-ray diffraction, LT "child" structure obtained by applying matrix to HT "parent" structure and LT structure determined by powder X-ray diffraction.

Our initial VT powder experiment was conducted on the "d9" diffractometer using a flat

plate sample under vacuum. However, the variable temperature PXRD patterns showed that CA-Pyz molecules underwent partial sample decomposition close to room temperature to form CA; probably because Pyz molecules are “pumped out” by the high vacuume in the cryostat. To overcome this, capillary experiments were used for data collection instead. Five capillary experiments were carried out on “d6” diffractometer and the experimental details are given in Table 3.3. It should be noted that the phase transition temperature (T_c) differs a little in each experiment. Since CA-Pyz was also found to decompose slowly at 400 K, the best experiment (d6b_00937) was to collect data at 65 temperatures between 120 K to 370 K in order to gain insight into the phase transition. From the RT PXRD data, it appears that a small amount (weight percentage of 8%) of chloranilic acid was present as an impurity in the sample.

Experiment	Process	T_{min} (K)	T_{max} (K)	Rate (K/hour)	T_c (K)	Data sets
d6b_00802	cooling	100	310	15	307	50
d6b_00803	warming	150	400	15	300	62
d6b_00929	cooling	120	400	3	270	103
d6b_00930	warming	120	400	4	270	73
d6b_00937	cooling	120	370	4	275	65

Table 3.3: Experimental details for variable temperature powder X-ray diffraction carried out on “d6”.

The variable temperature PXRD patterns obtained from the optimum experiment (d6b_00937) are shown in Figure 3.7. We only show 2θ from 3° to 20° where the most notable changes occur (see Table 3.5). The four peaks appearing at approximately 2θ 8.2°, 9.1°, 10.2° and 15.9° at 370 K changed dramatically upon cooling. In fact, each of these four peaks is an overlap of two reflections in the P-1 cell. For example, reflections (101) and (011) are perfectly superimposed for a cell with a=b and α=β (i.e. when it is perfectly equivalent to the C2/m cell). When the temperature is decreased, reflection (011) moves to smaller 2θ value (7.78°) while reflection (101) shifts to larger 2θ value (9.17°).

In addition, reflections (101) and (0-11) actually cross in 2θ on cooling, which is quite unusual. These observations indicate that CA-Pyz shows very large and anisotropic changes in cell dimensions on cooling.

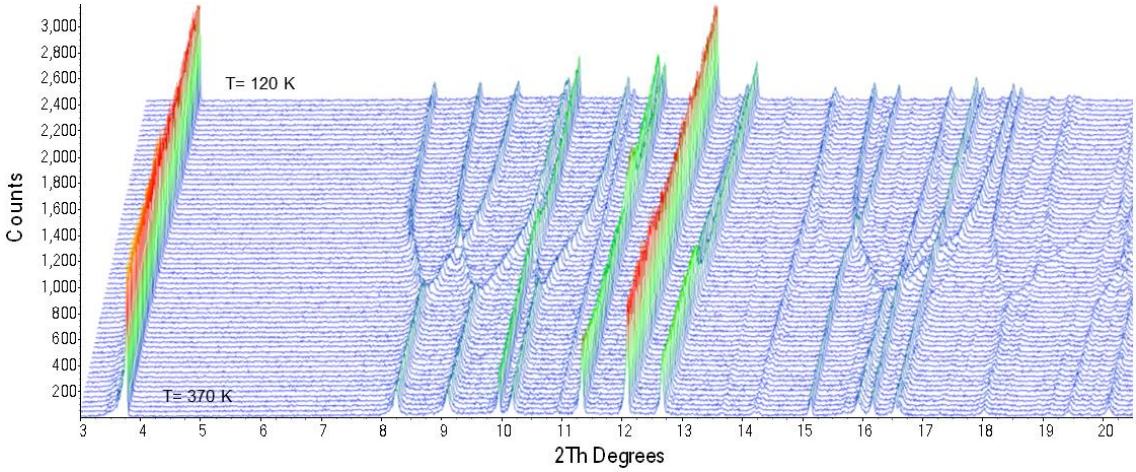

Figure 3.7: Variable temperature powder patterns obtained from experiment d6b_00937 collected in a "d6" capillary experiment.

Reflection	2θ degree (°) at 370 K	2θ (°) at 120 K
(101)	8.24	9.167
(011)	8.28	7.775
(10-1)	9.10	10.017
(0-11)	9.13	8.542
(102)	10.18	10.996
(012)	10.20	9.964
(211)	15.91	17.393
(121)	15.97	15.090

Table 3.5: Details of reflections and corresponding 2θ values at both 370 K and 120 K.

It is not feasible to follow the evolution of a structure as complex as CA-Pyz with temperature from powder data by freely refining atomic coordinates. Instead, we initially refined the data using a rigid body approach. The use of rigid bodies minimises the number of parameters refined. The rigid bodies were defined in terms of Cartesian coordinates, the xyz atomic position for each molecules, center of mass and by the rotation of each molecule around three perpendicular axes. These values were derived

from the LT single crystal structure model. Data collected from experiment (d6b_00803) was analysed in this way. During Rietveld analysis, the molecule position and 6 rotation angles were refined as allowed by symmetry. Chloranilic acid rotations around three perpendicular axes are described by 3 rotational parameters (ca_rotx, ca_y and ca_rotz) while rotations of pyrazine molecules are described by py_rotx, py_rotx and py_rotz. Other refined parameters included the unit cell dimensions (a, b and c), the unit cell angles (alpha, beta and gamma), any individual isotropic temperature factors for chloranilic acid and pyrazine molecules, 12 background coefficients, the sample displacement and 4 peak shape function parameters (pku, pkv, pkw and pky). The R_{wp} agreement as a function of temperature is shown in Figure 3.8. The R factor varies smoothly with temperature suggesting a similar quality of fit at each temperature.

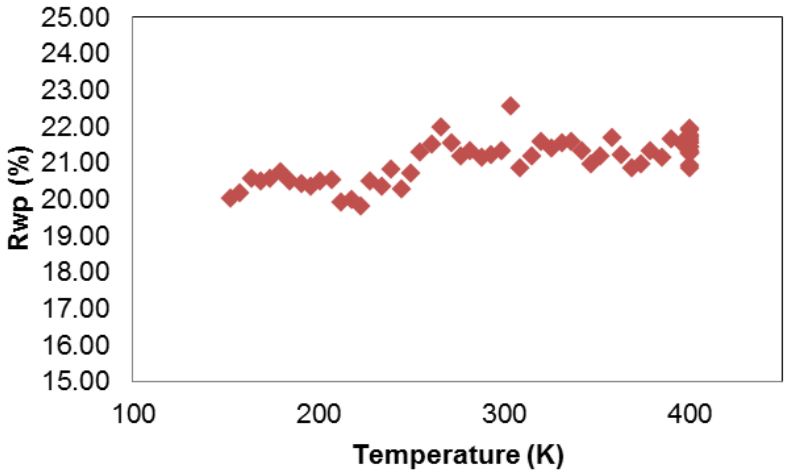

Figure 3.8: The value of R_{wp} change with temperature obtained from Rietveld refinements using rigid bodies.

Figure 3.9 and 3.10 show how the cell parameters vary with temperature. The unit cell parameter a and b changed very smoothly with temperature by 1.83% and 1.04% respectively in the temperature range of 150 K – 240 K, indicating the relatively normal thermal expansion. Then, the unit cell parameter a dropped significantly (~-9.73%) while the unit cell parameter b increased significantly (~+7.10%) between 240 K and 300 K. The phase transition temperature, T_c = 300 K, is defined by the temperature where the

two parameters a and b converged (Figure 3.9a). The unit cell parameter c (Figure 3.9b) elongated by +2.6% between 150 K and 300 K. The unit cell angles alpha and beta show more unusual behavior as given in Figure 3.10a. At low temperature alpha and beta differ by ~1°, but become equal above T_c (as expected for a C-centered monoclinic cell). Alpha appears to vary smoothly as T_c is approached whereas beta reaches a minimum value just below T_c before increasing. This suggests that two processes might be occurring (see also the discussion below). Similarly, gamma (Figure 3.10b) increases until 250 K, then falls just below T_c. The rotational angles of chloranilic acid and pyrazine molecules are plotted as a function of temperature in Figure 3.11. Pyrazine molecules mainly rotate around the z-axis. The rotational angle of pyrazine molecules increased with temperature and showed a significant change (approximately 25°) between LT and HT around the z-axis. Chloranilic acid molecules started to rotate around y- and z-axes at 250 K. The rotational angles of chloranilic acid molecules also increased with temperature by 5° which is 6 times smaller than pyrazine. As a result, the structural change in CA-Pyz crystal appeared to be dominated by pyrazine rotation.

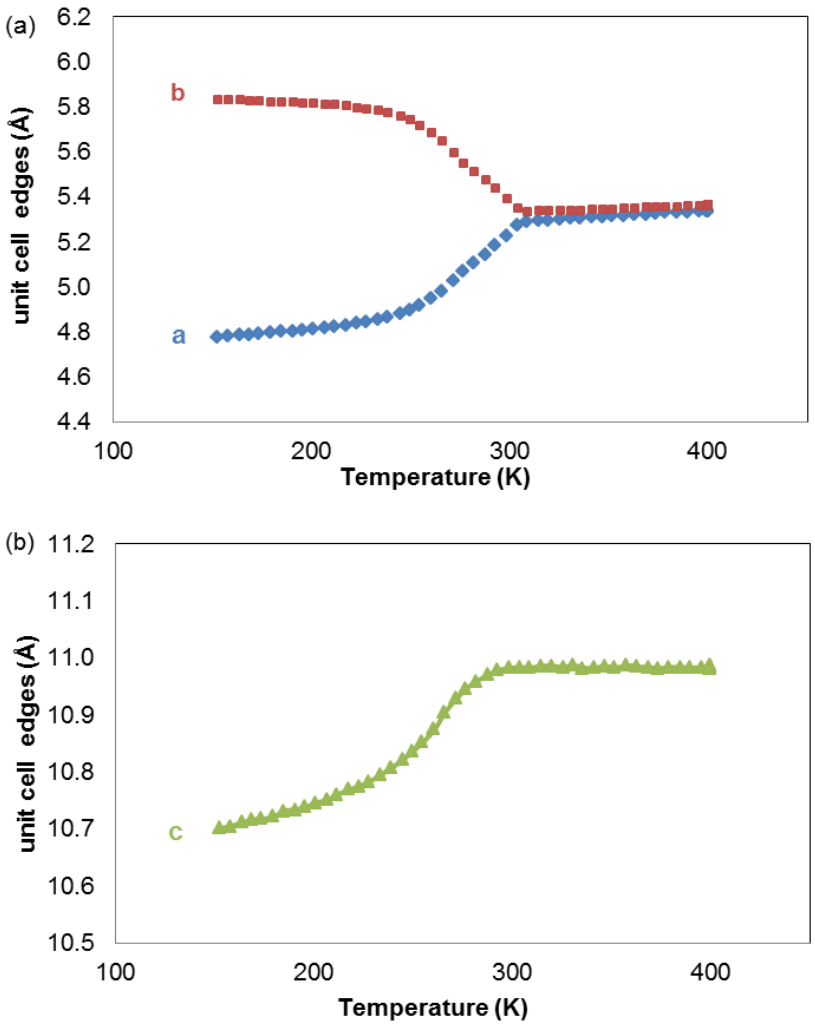

Figure 3.9: The unit cell dimensions changed as a function of temperature determined by variable temperature powder X-ray diffraction upon warming. (a) The unit cell dimension a and b. (b) The unit cell dimensions c.

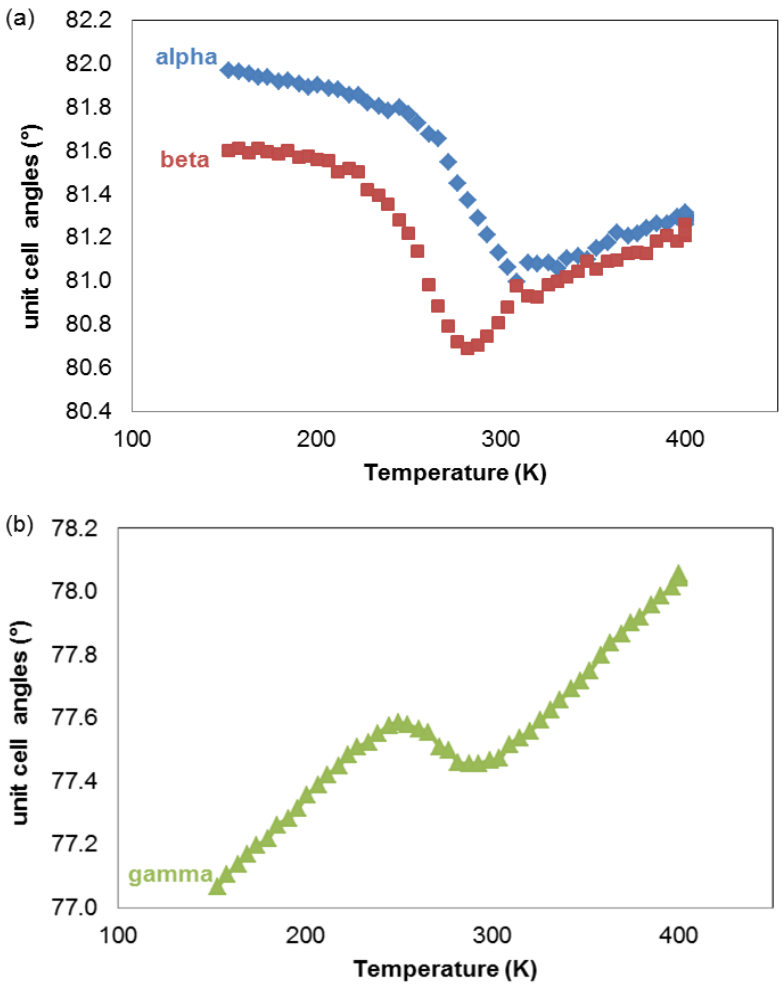

Figure 3.10: The unit cell angles changed as a function of temperature determined by variable temperature powder X-ray diffraction upon warming. (a) The unit cell angles alpha and beta. (b) The unit cell angle gamma.

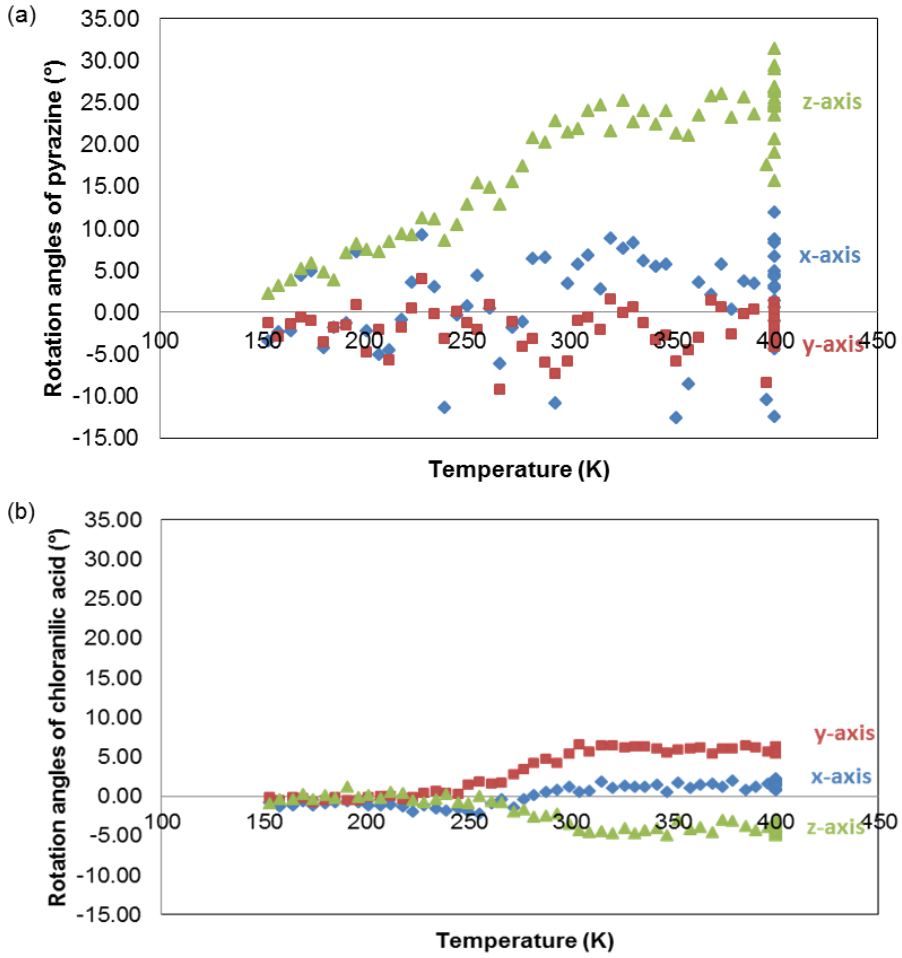

Figure 3.11: The molecular rotational angles as a function of temperature determined by the Rietveld fitting. (a) The rotational angles of pyrazine molecule and (b) the rotational angles of chloranilic acid molecule with respect to x,y and z axes.

3.3.3 Refinements of distortion-mode amplitudes

The analysis above is based on the use of traditional xyz crystallographic coordinates. For many structural phase transitions, it can be more helpful to use the idea of distortion mode amplitudes. In this method, structures are described not by fractional atomic coordinates but in terms of the parent high symmetry structure and the amplitude of distortion modes from this structure. The Rietveld refinement with distortion-mode description can help understand the essential features of distorted structure as they can often be described with just a small number of mode amplitudes. This has been done for a number of structural transitions and more recently extended to investigate magnetic transitions, where axial vectors are set up to describe magnetic spins.[79] It turns out that

the same language used to describe magnetic spins can be applied to describe the motion of rigid molecules. Better data collected from experiment d6b_00937 have been analysed in this way to investigate the distorted structure of CA-pyz. In this case, six molecular distortion-mode rotational amplitudes (r1-r6) are used to describe the rotations in the chloranilic acid pyrazine cocrystal. The chloranilic acid molecule rotations are described by r1, r2 and r3. Meanwhile, the rotation of pyrazine molecule is described by r4, r5 and r6. An axial vector (r3) describing the rotation of chloranilic acid is shown in Figure 3.12 as an example. The direction of the vector gives the rotation axis and its length gives the rotation magnitude. The 36 parameters (a1-a36) that could be used to describe the internal distortion of the molecule by moving its constituent atoms are fixed at zero in this approach. The LT structure model (P-1) as child of HT parent is used for fits to all temperatures.

In the first model, isotropic peak shape parameters were used. All six rotational amplitudes were refined at each temperature giving an average R_{wp} of 22.19% for the 65 data sets. A plot (Figure 3.13) of the refined distortion-mode amplitudes versus temperature shows the rotations of chloranilic acid and pyrazine molecules. All r1-r6 refined close to zero at high temperature as expected. At low temperature, r4 refined to a relatively high value (approximately 0.25 radian). It therefore appears that r4 plays a key role in structure distortion. Since r5 and r6 are scattered with large uncertainties, they perhaps are not needed to fit the data. If r5 and r6 are fixed at zero, the average R_{wp} (22.22%) almost remains unchanged. As a result, r5 and r6 are not necessary for fitting low-temperature structure.

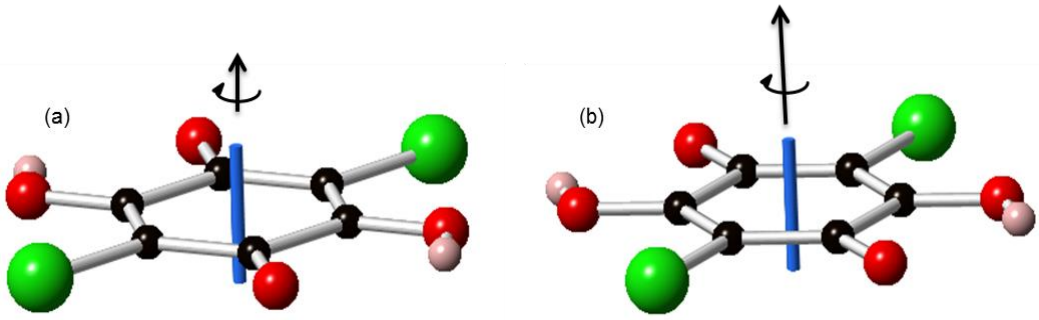

Figure 3.12: The rotations at (a) 1 degree and (b) 24 degree of chloranilic acid around axial distortion-mode amplitude r3.

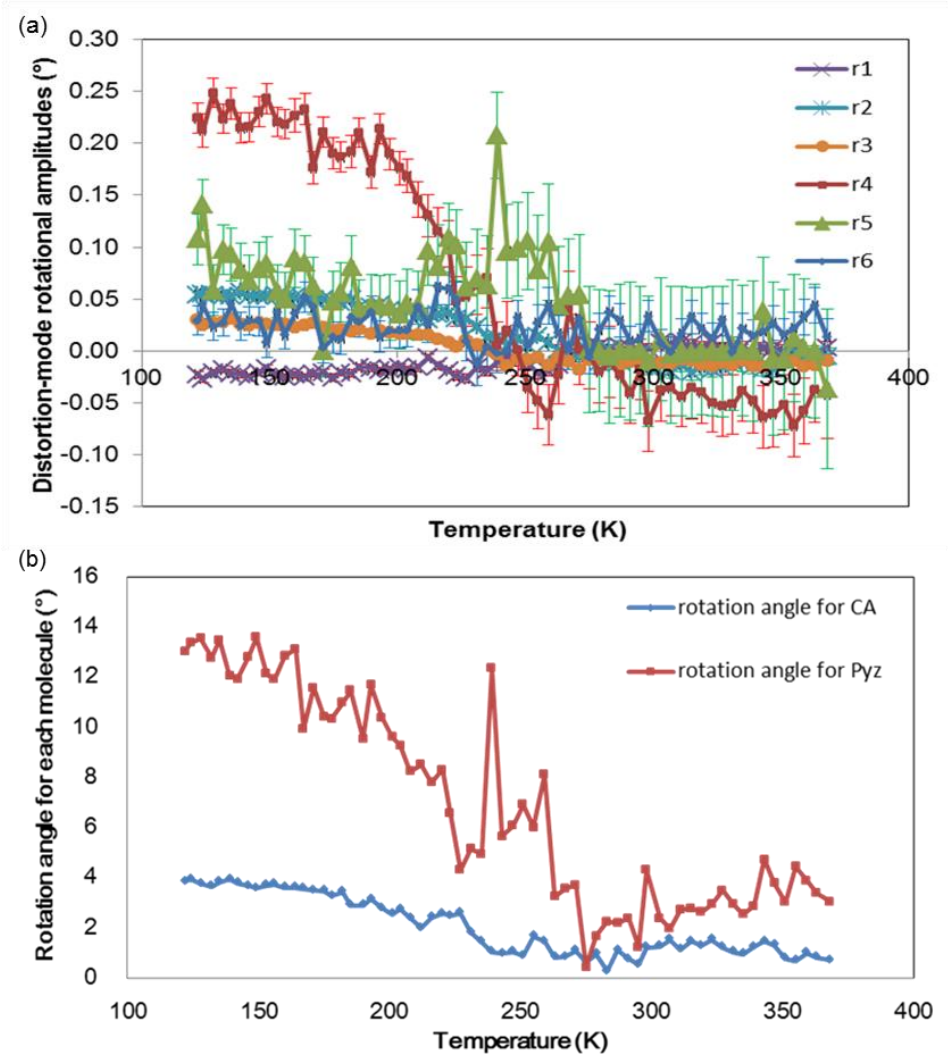

Figure 3.13: (a) The temperature dependence of molecular distortion mode rotational amplitudes (r1-r6) obtained from the Rietveld refinements using the low-temperature P-1 model as child of high-temperature parent. (b) The overall rotation angles for chloranilic acid and pyrazine molecules.

The second model used was the one in which a simple anisotropic peak shape was used. For this we used the Stephen's peak model which is an hkl-dependent strain correction to the peak shape. Only three additional peak shape parameters (s040c, s400c and s220c) are refined at low temperature then fixed at these obtained values for all other temperatures. The fits are slightly improved with an average R_{wp} of 20.42%. However, the fit (range 30, Figure 3.14a) close to T_c giving R_{wp} of 22.93% is not as good as fits at HT (range 1, Figure 3.14b) and LT (range 65, Figure 3.14c). This is also shown by the R_{wp} plot of Figure 3.15. It again provides a hint that the sample behavior close to T_c is unusual. It is worth noting that these effects are more clear than in analysis of the lower

quality data represented by Figure 3.8.

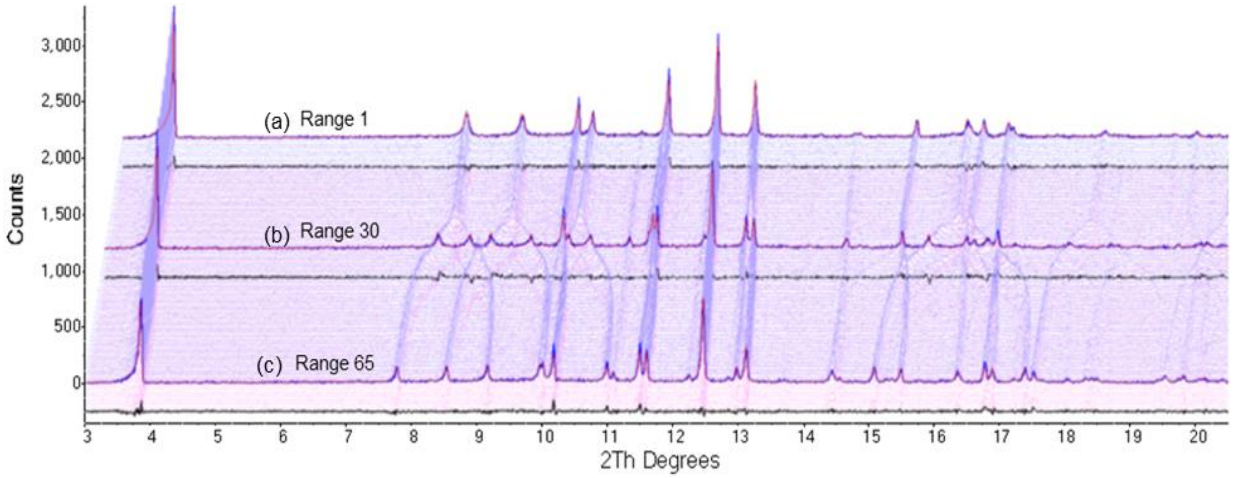

Figure 3.14: The Rietveld fits to (a) range 1 at 370 K, (b) range 30 close to 275 K and (c) range 65 at 120 K. The data sets were obtained from variable temperature capillary experiment and analysed by refinements with distortion-mode amplitudes using P-1 structure model

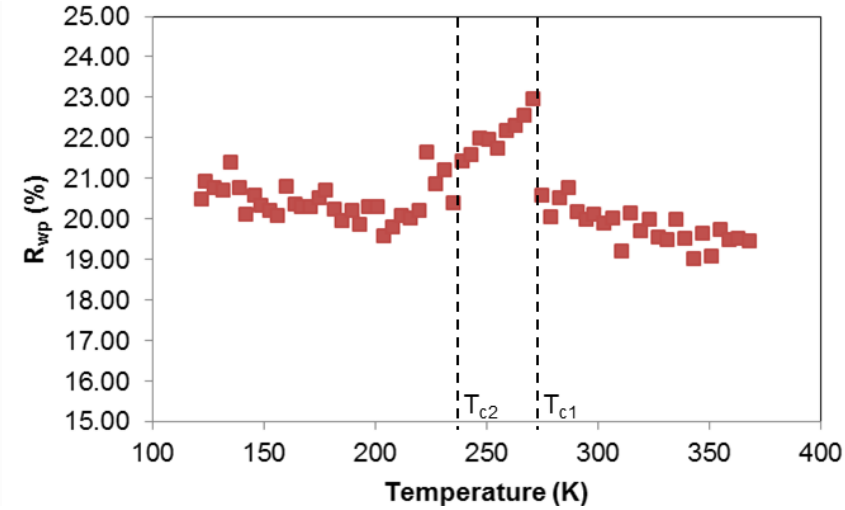

Figure 3.15: The value of R_{wp} changes with temperature obtained from the Rietveld refinements using a simple anisotropic peak shape model.

The unit cell parameters and the distortion-mode amplitudes are all plotted as a function of temperature in Figures 3.16 and 3.17. The unit cell parameters a and b (Figure 3.16a) become equal at T_{c1} of 275 K as do the unit cell angles alpha and beta (Figure 3.16b). As before, angles alpha and beta showed unusual behaviour between T_{c2} (235 K) and T_{c1} (275 K). The higher quality data also show a small discontinuity in a and b cell parameters around 235 K. The phenomenon observed in the plot of Rwp versus

temperature is also consistent with the behavior of the unit cell angle beta between 230 K and 275 K. The plot (Figure 3.15) of distortion-mode amplitudes versus temperature presents the rotations of chloranilic acid and pyrazine. The distortion-mode amplitude r4 changes the most (~0.2 radian) among the four amplitudes. It also shows a sudden jump at ~260 K and then decreases with fluctuation.

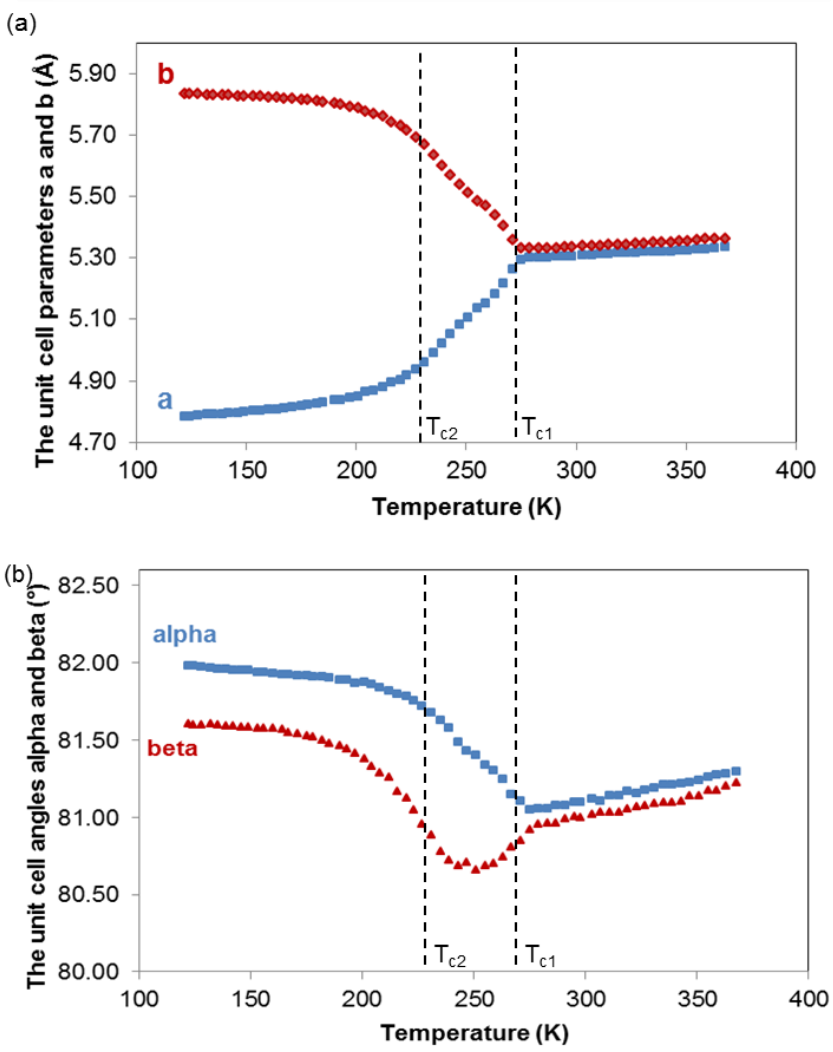

Figure 3.16: The unit cell parameters trends as a function of temperature determined by variable temperature X-ray diffraction upon cooling using Rietveld refinements with a simple anisotropic peak shape model.

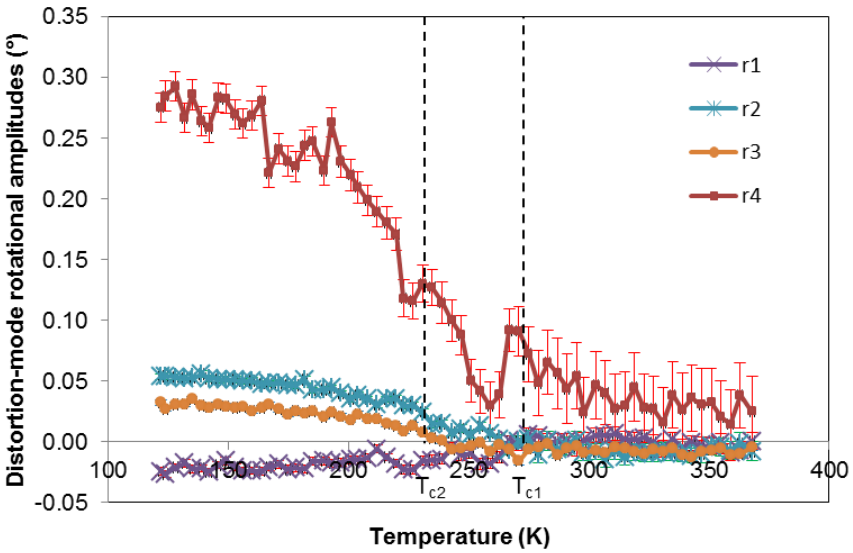

Figure 3.17: The temperature dependence of molecular distortion mode rotational amplitudes (r1-r6) obtained from the Rietveld refinements using low-temperature P-1 model as child of high-temperature parent.

We can gain significant insight into what's happening in this system by seeing how the R_{wp} of refinements are influenced by the mode amplitudes that are refined. Figure 3.18a shows the difference in R_{wp} for each temperature for a model with all r1-r6 refined versus one in which r5 and r6 are fixed. From the tiny change in R_{wp}, we can conclude that modes r5 and r6 are not important in describing the phase transition. Figure 3.18b compares a refinement in which all r1-r6 are refined and a refinement in which CA modes r1-r3, r5 and r6 are fixed. Here we see that the difference in R_{wp} only rises below 235 K, suggesting that CA motion is only important below a lower critical temperature T_{c2} of 235 K. Finally, Figure 3.18c show the difference in R_{wp} between a refinement in which all r1-r6 are refined and a refinement in which all amplitudes are fixed. Here we see that Pyz movement appears to be needed at temperature below T_{c1}=275 K. These temperatures are shown as dashed lines in Figures 3.15 to 3.18.

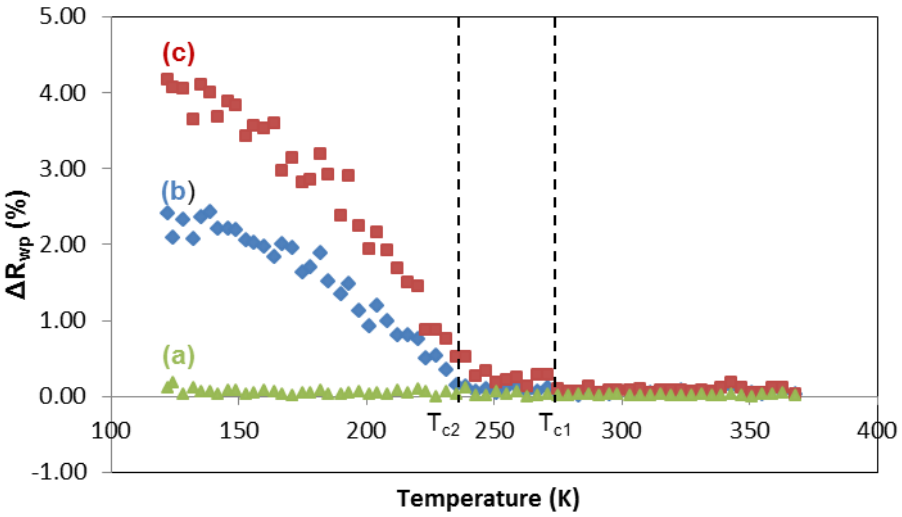

Figure 3.18: Difference in R_{wp} for each temperature. (a) The difference in R_{wp} between the model with all r1-r6 refined and the model with r5 and r6 fixed. (b) The difference in R_{wp} between the model with all r1-r6 refined and the model with r1-r3, r5 and r6 fixed. (c) The difference in R_{wp} between the model with all r1-r6 refined and the model with all r1-r6 fixed.

It is the first time that refinements of molecular distortion modes have been used to investigate crystal structure of any molecular structure. Those distortion-mode amplitudes can quantify the phase transition from parent structure to distorted child structure via rotational mode amplitudes. Variable temperature data can be refined using a simple model with only three anisotropic peak shape parameters. The structure distortion can be mainly described by molecular distortion-mode rotational amplitude r4. That is, the rotation of pyrazine molecules drove the phase transition that occurred in the CA-Pyz crystals. The outcome is consistent with the result (Figure 3.10) obtained from the Rietveld refinement with rigid bodies.

3.4 Summary

The neutral 1:1 cocrystals of chloranilic acid and pyrazine were successfully obtained by slow evaporation. An extensive study of whether chloranilic acid-pyrazine undergoes a ferroelectric phase transition was carried out. The crystal structures at both HT and LT were determined by single crystal X-ray diffraction. The HT structure belongs to centrosymmetric space group C2/m and undergoes a phase transition to the LT structure

that belongs to another centrosymmetric space group $P\bar{1}$. The temperature dependence of the unit cell parameters and the molecular distortion-mode rotational amplitudes were obtained from powder X-ray diffraction. The phase transition is driven by the distortion-mode amplitude r4 of pyrazine molecule which captures most of the effect. By comparing the R-factors for each temperature, it suggests that pyz movement becomes important at T_{c1}=275 K and CA movement becomes important at T_{c2}=235 K

Chapter 4 Structural Investigation of Ferroelectric 2-Methylbenzimidazole

4.1 Introduction

Imidazole is an aromatic heterocyclic compound which plays an important role in biological systems. In the solid state, imidazole motifs are typically connected by intermolecular hydrogen bonds. As discussed in Chapter 1, croconic acid is a prototypical high-performance single-component ferroelectric in which proton transfer is responsible for the ferroelectricity. 2-Methylbenzimidazole (2-MBI) was proved to be a hydrogen-bonded molecular system exhibiting above-room-temperature ferroelectricity.[3] As a single-component ferroelectric, 2-MBI (Figure 4.1) can work as both proton donor and acceptor because it contains proton-donating group NH and proton-accepting atom N. The proton transfer mechanism (Figure 4.2) under an applied electric field resulting in a reversal in polarisation was suggested as being responsible for the ferroelectricity in 2-methylbenzimidazole.[80, 81] The P-E hysteresis loops (Figure 4.3) measured at 298 K validated its ferroelectricity.[3] It exhibited a large remanent polarisation of 5.2 $\mu C/cm^2$. When polarisation is 0, the coercive field was determined to be 11 kV/cm at 0.2 Hz and increased with frequency.

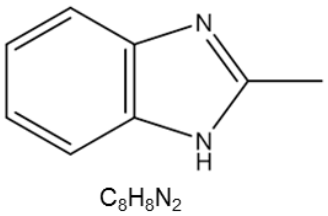

$C_8H_8N_2$

Figure 4.1: Molecular structure and chemical formula of 2-methylbenzimidazole.

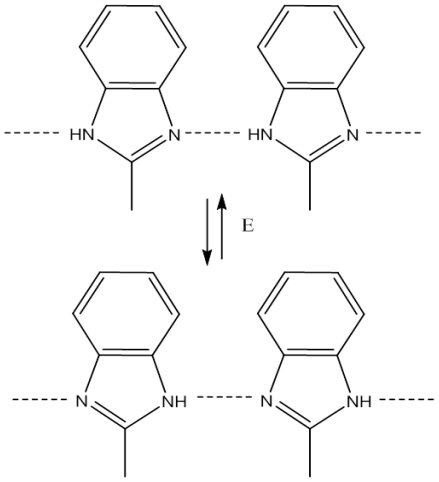

Figure 4.2: The proposed proton transfer mechanism between 2-methylbenzimidazole molecules under an external electric field.

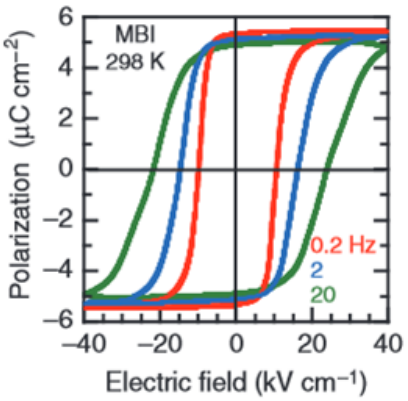

Figure 4.3: P-E hysteresis loops measured for 2-methylbenzimidazole at room temperature.[3]

A paper published in 1991 reported the crystal structure of 2-MBI solved by direct methods.[82] The material, crystallising in tetragonal space group $P4_2/n$, was investigated by single crystal X-ray diffraction. In the $P4_2/n$ structural model, protons are disordered (Figure 4.4a), since they can be bonded to the two equivalent nitrogen atoms with equal probability. In contrast, a recent work[3] suggested that the crystal structure is in low-symmetry monoclinic space group Pn and that the structure appeared tetragonal because the single crystal was in a multi-domain state. The structure (Figure 4.4b) was only investigated at 300 K using synchrotron X-ray diffraction, and the protons were found to be fully ordered, pointing in the same direction parallel to the [-1 1 0] of the Pn cell. The reported Pn structure possessed good quality with R and R_w equal to 4.59% and 5.54% respectively. However, the publication did not give any indication of the treatment

of twinned domains. The piezoresponse force microscopy (PFM) measurement demonstrated the multiple ferroelectric domains that are related by 90° rotations with respect to each other.

The purpose of this work was to investigate whether 2-MBI undergoes any structural phase transition in its stability range, especially to a paraelectric centrosymmetric structure. The experiments included variable temperature powder and single crystal X-ray diffraction and variable temperature solid-state NMR, as well as calculations of the proton NMR spectra.

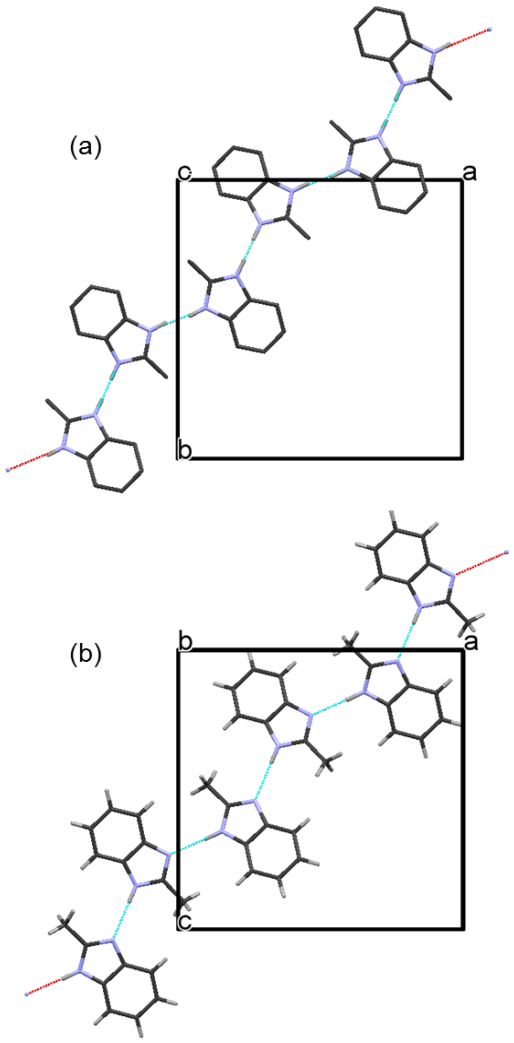

Figure 4.4: Crystal structures of 2-MBI from the Cambridge Structural Database obtained at room temperature. (a) Projection of the tetragonal ($P4_2/n$) 2-MBI structure down the c-axis, refcode KOWYEA. Note that not all H atoms are given in this cif. (b) Projection of the monoclinic (Pn) 2-MBI structure down the b-axis, refcode KOWYEA02. Colour legend: black-C; grey-H; blue-N. Turquoise dotted lines represent hydrogen bonds. Only one chain in the plane and along the stacking axis is shown for clarity.

4.2 Experimental details

4.2.1 Sample preparation

2-MBI (98%) was purchased from Aldrich. For powder diffraction and solid-state NMR, this material was used without further purification. Single crystals of 2-MBI were grown from alcohol (methanol, ethanol and 2-propanol) solutions at room temperature. 2-MBI (0.0264g, 0.2 mmol) was dissolved in 6 ml of solvents with gentle stirring. Colourless needle-shaped crystals were obtained from the methanol solution after three days. One week later, crystals also appeared in both ethanol and 2-propanol solutions.

4.2.2 Single crystal diffraction

An Oxford Gemini S Ultra diffractometer with a CCD detector was used to collect data at 120 K and 290 K using Mo Kα radiation (λ=0.71073 Å). Two-component glue was used to attach the crystal to a glass fibre which was then mounted on a metal pin. After that, the pin was placed on a goniometer head and then the goniometer head was put on the diffractometer. The exposure time was 20 seconds per frame. A Cryostream Plus Controller was used to control the experimental temperature. All non-hydrogen atoms were refined anisotropically, while all hydrogens were located by difference Fourier maps and refined isotropically. A default SIR92[66] structure solution software was used within the CRYSTALS[67] software. A three parameter Chebyshev weighting scheme was applied.

4.2.3 Powder X-ray diffraction (PXRD)

To determine the phase identity and identify possible phase transitions, both flat plate and capillary PXRD experiments were carried out (Table 4.1). Quick (30-minute) patterns were recorded from 5-50° using a step size of 0.02° on a Bruker D8 ADVANCE diffractometer equipped with a Cu tube (d7) at room temperature. The diffraction slides were covered with a thin layer of Vaseline as an adhesive. Then, finely ground crystals were sifted onto the silicon flat plate through a 120 mesh sieve. The plate was put into

diffractometer with knife edge fitted on. Also, a Bruker D8 diffractometer equipped with a Mo tube (d6) was used to carry out variable temperature measurements on 2-MBI, collecting a series of 20-minute scans from 1-30° with a step size of 0.01°. Ground and sifted 2-MBI powders were packed into a 0.7 mm borosilicate glass capillary to a length of 35 mm. The capillary was flame-sealed and then placed in a 1 mm internal-diameter 5 mm external-diameter 20 mm-length capillary tube using superglue. After that, the capillary which was placed in the capillary tube was attached to the goniometer head. The Cryopad software was used to control the Oxford Cryosystems Cryostream, and control the experimental temperature.

Experiment	Flat plate	Capillary
Instrument	“d7”	“d6”
2θ range(º)	5-50	1-30
Step size(º)	0.02	0.01
Time per scan (min)	40	55
Temperature (K)	290	400 - 150
No. of data sets	1	52

Table 4.1: Experimental parameters of powder X-ray diffraction for 2-MBI.

4.2.4 SSNMR

Carbon and proton spectra were both recorded on a Bruker Avance III HD spectrometer using magic-angle spinning probes. Carbon spectra were collected from 170 K to 420 K using a 4 mm HX MAS probe with spin-rate of 7 kHz. Proton spectra were collected from 100 K to 385 K using the 4 mm HX MAS probe used for carbon spectra but with spin-rate of 14 kHz. For investigating any possible structural changes, proton spectra were recorded by direct excitation method using a 1.9 mm HX MAS probe with the spin-rate of 40 kHz from 213 K to 297 K.

4.2.5 Computational methods

Two structural models (Pn and $P4_2/n$) of 2-MBI were used to calculate the proton spectra. To optimise geometry, Perdew-Burke-Ernzerhof (PBE) parameterisation[83] was utilised for the exchange-correlation (xc) functionals. In those calculations, the magnetic shielding was computed. All the simulations were carried out within the density functional theory (DFT) using CASTEP[84] programme.

4.3 Results and discussion

4.3.1 Variable temperature powder X-ray diffraction

In order to detect any potential structural changes, samples of 2-MBI were investigated by powder XRD between 400 K and 120 K. Variable temperature powder XRD data were analysed by Rietveld fitting[70] using Topas Academic[71], in which the fractional atomic parameters were fixed using the $P4_2/n$ model obtained from the Cambridge Structural Database (CSD). The refined parameters included the unit cell parameters, an overall isotropic temperature factor, the sample zero point, the background coefficients and the peak shape function parameters. The unit cell parameters and the unit cell volume are all plotted as a function of temperature in Figure 4.5. The blue data points corresponding to cooling data are superimposed over the red warming data points, which show the reversible thermal expansion and contraction changes in the unit cell. It is worth noting that unit cell dimension a (Figure 4.5a) changed by approximate 0.42% while unit cell parameter c (Figure 4.5b) changed by approximate 4.83% from 120 K to 400 K. It appears that the curve of unit cell volume versus temperature (Figure 4.5c) shows a possible small change of slope at approximately 250 K. As the reported crystal structure was only obtained from 300 K data, the question of whether the structure changes upon cooling or warming remains. To gain insight into the possible phase transition around 250 K, the crystal structure determination of 2-MBI at 120 K and 290 K was carried out using single crystal X-ray diffraction.

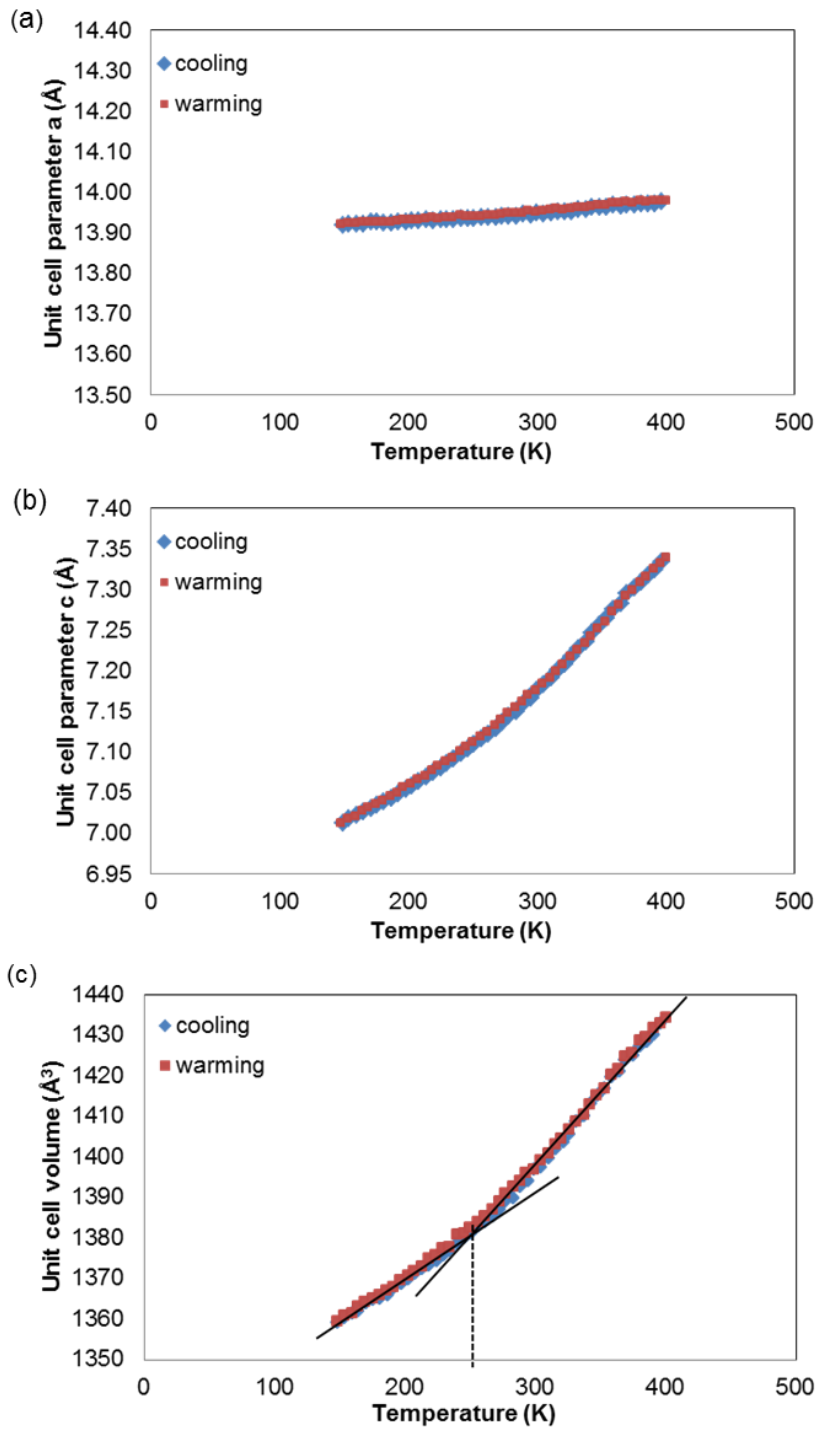

Figure 4.5: The temperature dependence of (a) the unit cell parameter a (=b), (b) the unit cell parameter c and (c) the unit cell volume of 2-MBI determined by variable temperature powder X-ray diffraction. The estimated standard uncertainties are 0.001 (a), 0.0005 (c) and 0.2 (volume).

4.3.2 Single crystal X-ray diffraction

The results (see table 4.2) obtained from single crystal diffraction identified the approximate structures at 120 K and 290 K which appeared to be tetragonal (space group $P4_2/n$) and unchanged upon warming except for the effects of the thermal expansion. Refinements using the monoclinic model (Pn, Z=4) was attempted. The twin law suggested by Rotax, a 90° rotation, was introduced into the refinement. However, this did not lead to a significant reduction in the R-factor (only 0.3%) and the quality of the model did not improve. Since the literature[3] suggest complex and multiple twinning , perphaps this two component twinning model was not sufficient. The refinements were therefore carried out in space group $P4_2/n$. Both crystal structures measured at 120 K (Figure 4.6) and 290 K exhibit disorder in which hydrogen atoms are equally distributed on both sides of the two-fold axis. Two 2-MBI molecules are connected by an N-H⋯N bond (Table 4.3). The unit cell dimensions a and b only expanded by 0.26% between 120 K and 290 K, and the unit cell dimension c expanded by 2.7%, ten times more than a and b. The reason for the large difference in thermal expansion can be seen from Figure 4.6. Hydrogen bonding occurs between two 2-MBI molecules in the (ab) plane, which restricts the motions of the molecules. The layers of hydrogen–bonded 2-MBI molecules stack along the c-axis without any significant intermolecular interactions. As a result, the unit cell was able to elongate along crystallographic c-axis more than both a and b directions. This is also consistent with the plots of unit cell parameters versus temperature shown in Figure 4.5.

	120 K	290 K
Chemical formula	$C_8H_8N_2$	$C_8H_8N_2$
Mr	132.16	132.16
Crystal system	Tetragonal	Tetragonal
Space group	$P4_2/n$	$P4_2/n$
Z	1	1
a (Å)	13.9147 (8)	13.9506 (9)
b (Å)	13.9147 (8)	13.9506 (9)
c (Å)	6.9870 (6)	7.1758 (7)
α (º)	90	90
β (º)	90	90
γ (º)	90	90
Volume ($Å^3$)	1352.81 (17)	1396.55 (19)
No. of measured reflections	15251	7285
No. of observed reflections	1412	716
No. of parameters	127	127
R, Rw (%)	9.507, 9.614	9.295, 9.790
I/Sigma cutoff	2	2

Table 4.2: Crystallographic data of chloranilic acid pyrazine collected at 120 K and 290 K.

	120 K	290 K
N-H distance (Å)	0.85 (2)	0.86 (2)
N…N distance (Å)	2.826 (4)	2.864 (4)

Table 4.3: Hydrogen bonds distances for 2-MBI at 120 K and 290 K.

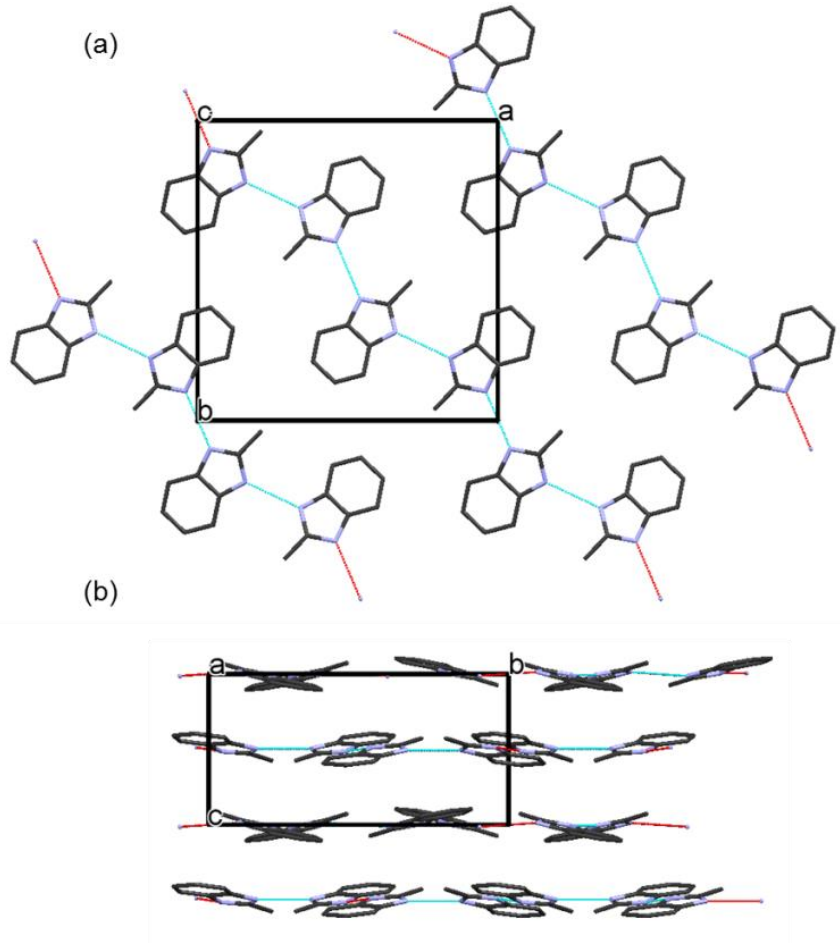

Figure 4.6: Crystal structures of 2-MBI obtained at 120 K from single crystal X-ray diffraction viewed along (a) stacking c-axis and (b) crystallographic a-axis and. Colour legends: black-C; grey-H; blue-N. The hydrogen bonds are represented by turquoise dotted lines. Hydrogen atoms have been omitted for clarity.

4.3.3 Solid-state NMR

Because X-ray diffraction may not be very sensitive to phase transitions arising mainly from the behaviour of protons, further evidence of whether the structure remains unchanged in the temperature range investigated was obtained from solid-state NMR. Carbon and proton spectra were measured at several temperatures between 170 K and 350 K. In carbon spectra (Figure 4.8), the chemical shifts did not vary significantly with temperature. Similarly, in proton spectra (Figure 4.9), there was not much movement of the proton signals. The peak with highest chemical shift was moved by only 0.6 ppm to a higher frequency. The other two peaks with lower frequency were only shifted by approximately 0.3 ppm. Solid-state NMR, therefore, provided additional evidence that

the structure of 2-MBI is unchanged in the temperature range of 170 K ~ 350 K.

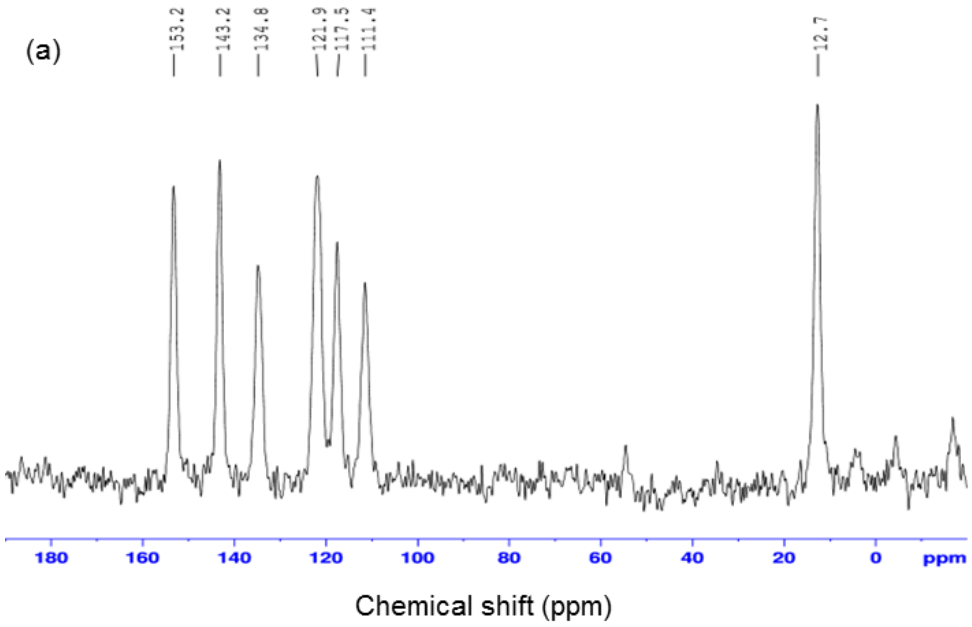

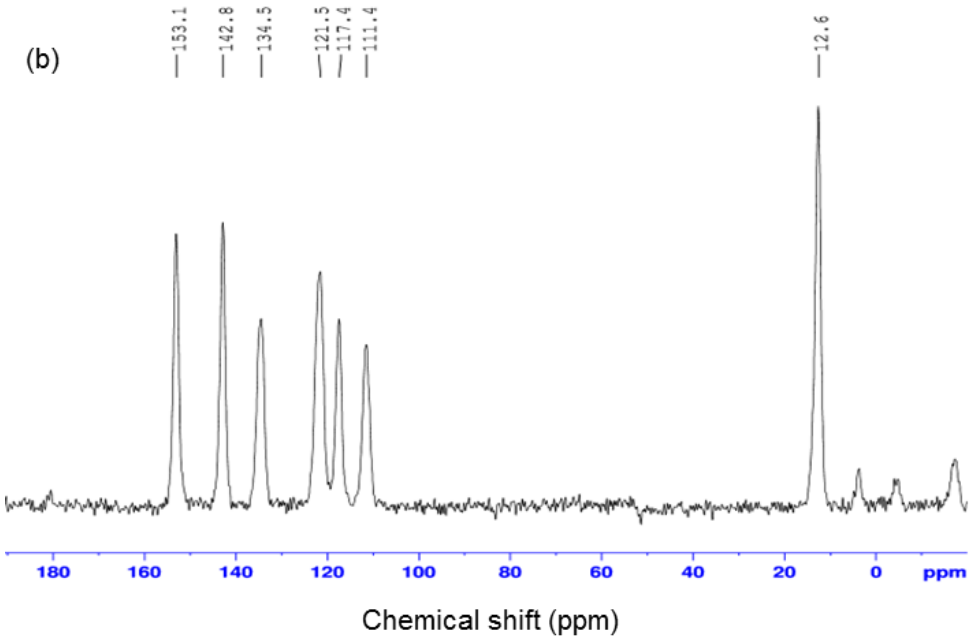

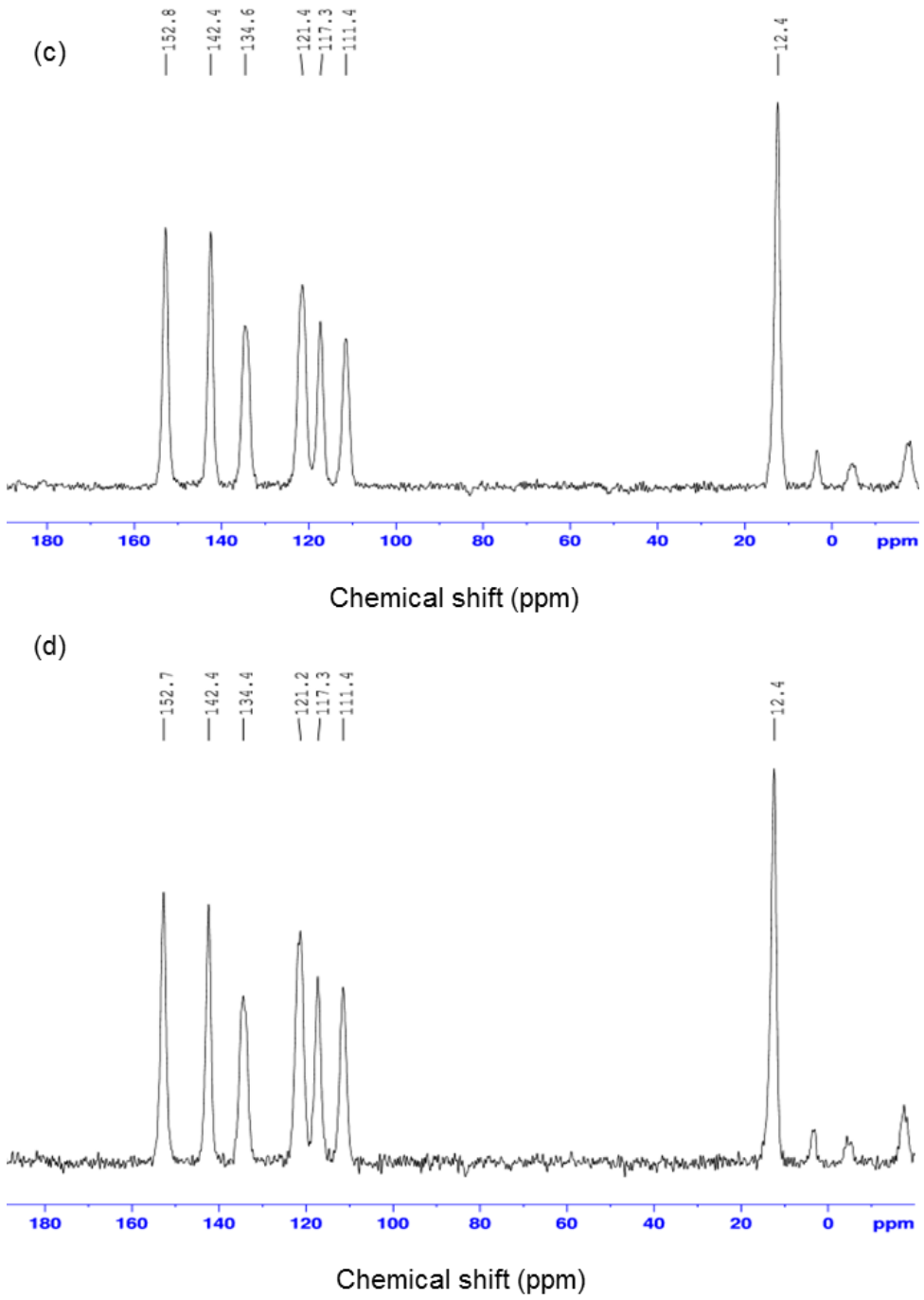

Figure 4.**7**: Carbon spectra of 2-MBI crystals obtained from solid-state NMR (a) at 165 K, (b) at 195 K, (c) at 295 K and (d) at 395 K.

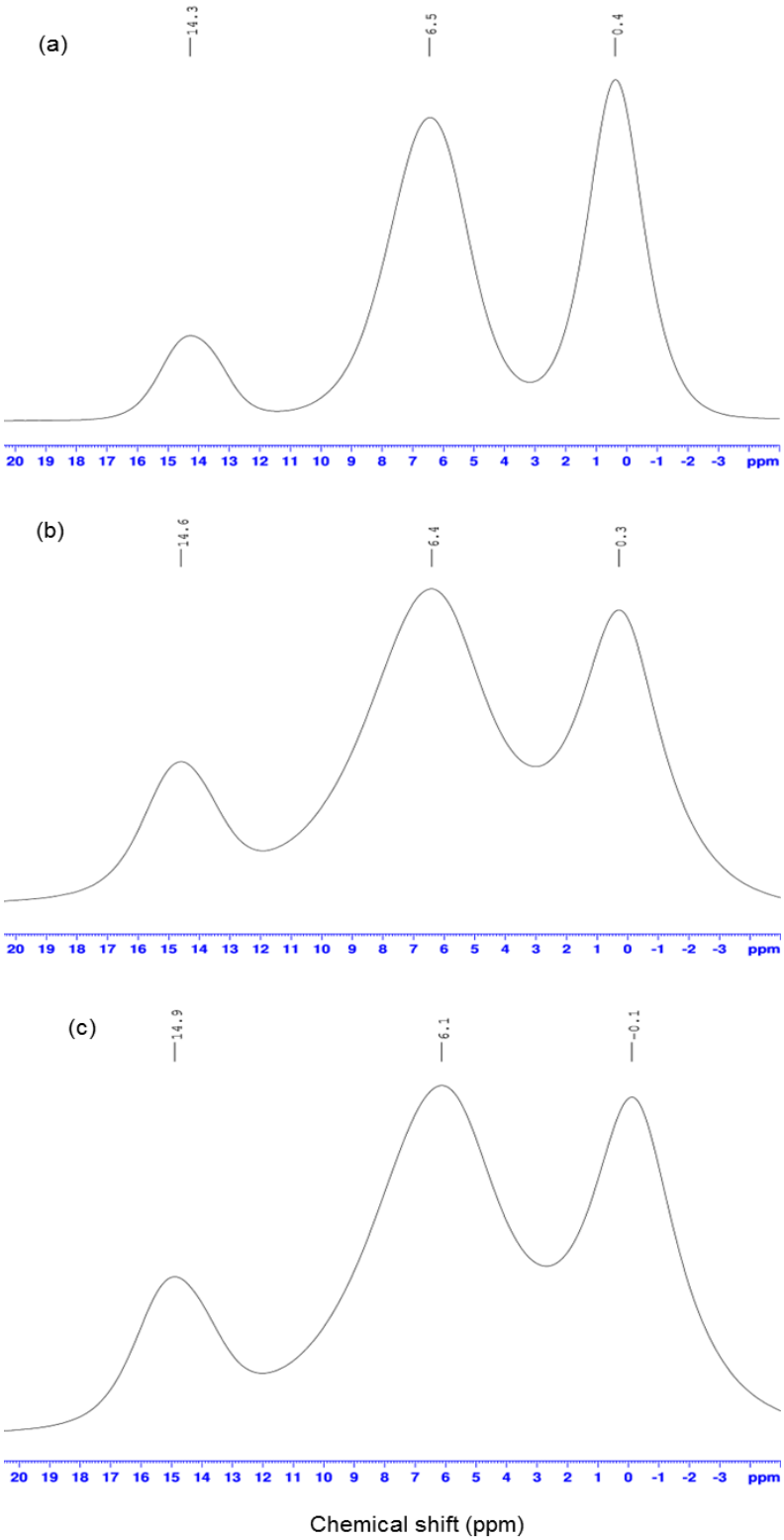

Figure 4.8: Proton spectra of 2-MBI crystals obtained from solid-state NMR at decreasing temperature (a) above room temperature with 40 kHz spinning, (b) above room temperature with 20 kHz spinning and (c) approximate 220 K with 20 kHz spinning

4.3.4 Proton spectra calculations

Finally, because the proton spectra should be very sensitive to the different arrangements of hydrogen atoms (in space groups $P4_2/n$ and Pn, Figure 4.4)， further supporting information for the space group was obtained from proton spectra simulations carried out in the CASTEP programme. Three different models were used to calculate the proton solid-state NMR spectra (Figure 4.9). Because the DFT calculations cannot deal with partially occupied sites, two models were derived from the tetragonal $P4_2/n$ structure, one (Model 1) in which the hydrogen-bonded protons are all bonded to nitrogen N1 (Figure 4.10a) and the other (Model 2) in which protons are all on nitrogen N2 (Figure 4.10b). These two models represent the extremes of the disordered crystallographic model in space group $P4_2/n$. It is important to note that these are both centrosymmetric models. The third model (Figure 4.10c) corresponds to the noncentrosymmetric and polar arrangement in space group Pn. The results of the calculated proton spectra are shown in Figure 4.11. The two calculated proton spectra indicated by the blue line and the green line represent the tetragonal Model 1 and Model 2 respectively. These two proton spectra are very similar in which two well-resolved signals appeared at approximately -30 ppm and -24 ppm. The proton spectrum calculated by Pn structure model, indicated by the pink line, differs from others by the peak occurring at approximate -15 ppm. In comparison to the experimental proton spectra, only monoclinic space group Pn provided the calculated proton spectrum that is similar to the experimental one. The result suggested that the real structure of 2-MBI is close to the monoclinic Pn model, at least on a local length scale.

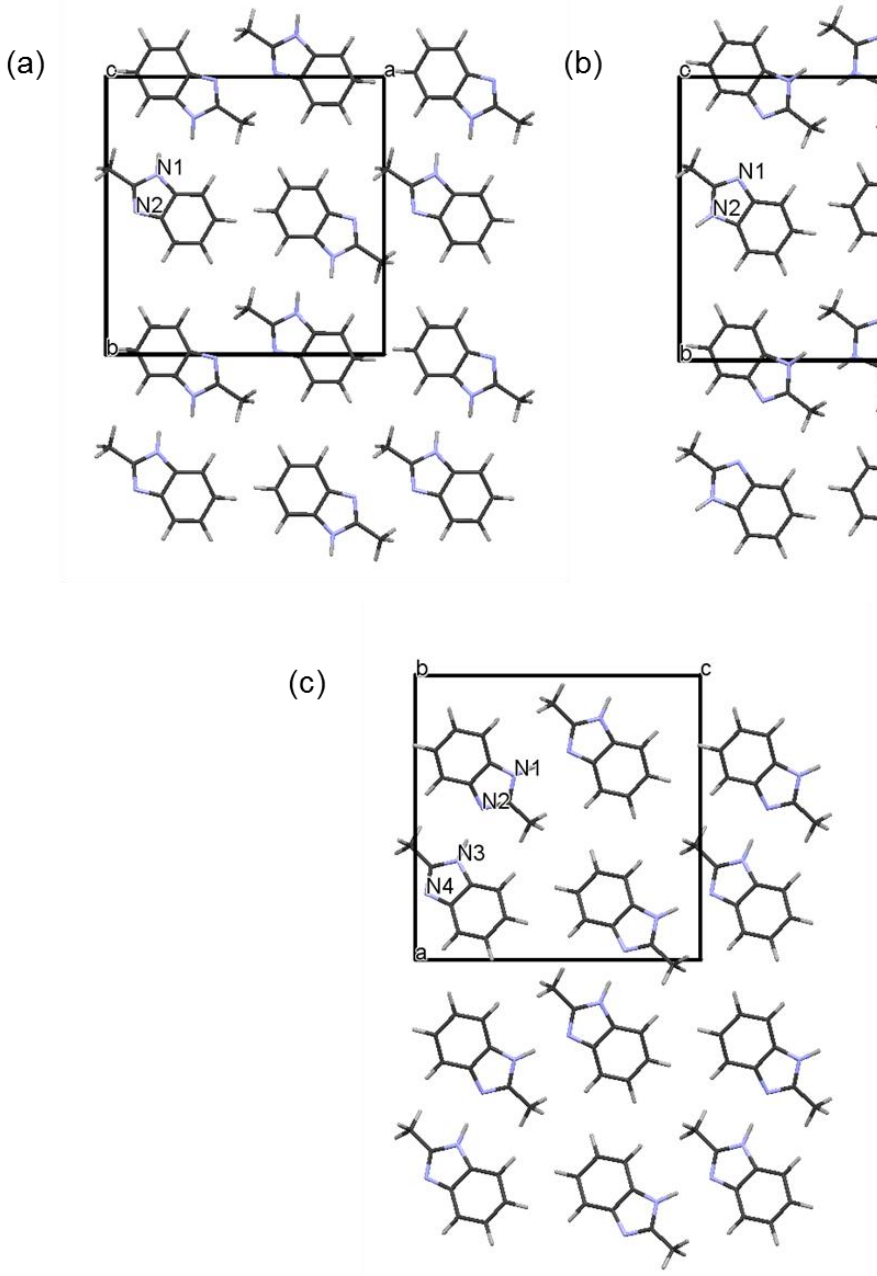

Figure 4.9: Crystal structures used for proton spectra calculations. (a) The structure in tetragonal space group $P4_2/n$ with protons all bonded to nitrogen N1 (Model 1). (b) The structure in tetragonal space group $P4_2/n$ with protons all bonded to N2 (Model 2). (c) The structure in monoclinic space group Pn (Model 3). Colour legends: black-C; grey-H; blue-N.

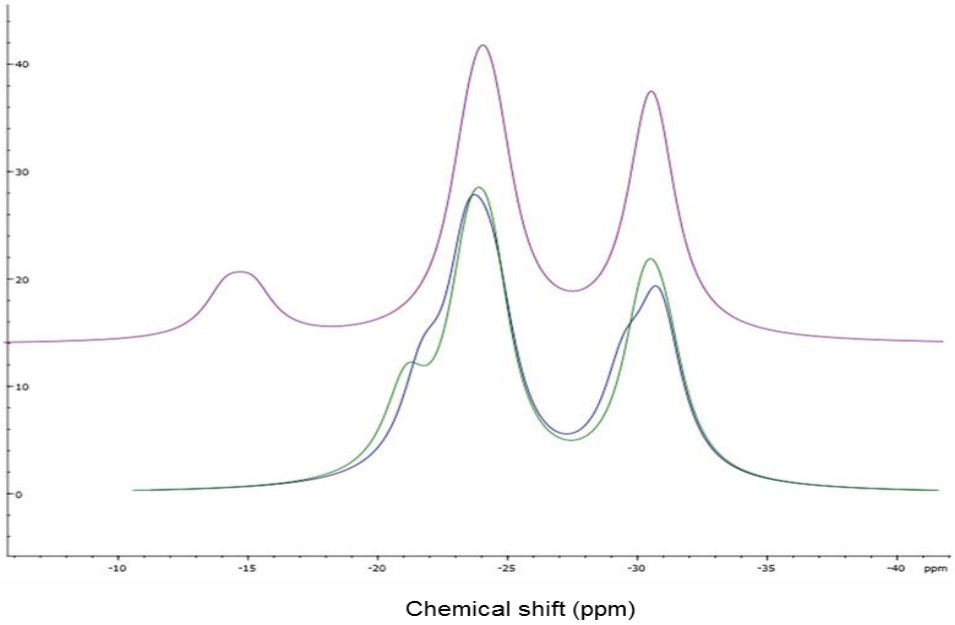

Figure 4.10: Calculated proton spectra obtained from CASTEP programme.

4.4 Summary

Apart from the influence of thermal expansion and contraction, the unit cell of 2-methylbenzimidazole did not exhibit significant changes in the temperature range of 120 K-400 K which was proved by the results obtained from variable temperature powder X-ray diffraction, variable temperature single crystal X-ray diffraction and the variable temperature solid-state NMR. The unit cell parameter c increased by 2.70% which was ten times more than unit cell parameters a and b did. The strong hydrogen bonding interactions occurring in crystallographic (ab) plane account for the behaviour of unit cell parameters. Also, the likely space group of 2-MBI was investigated by proton spectra calculation using CASTEP programme. The structure of 2-MBI was reported to be either centrosymmetric space group $P4_2/n$ or noncentrosymmetric space group Pn. The proton spectra calculated from both models providing the supporting information identified the space group of 2-MBI to be monoclinic noncentrosymmetric Pn.

Chapter 5 Conclusions and future works

This research involved the synthesis and structural investigation of the two-component chloranilic acid pyrazine crystal and the single-component ferroelectric 2-metylbenzimidazole. The crystal structure of chloranilic acid pyrazine determined by single crystal X-ray diffraction at 120 K was triclinic, P-1, with a=4.7684(2) Å, b=5.8402(3) Å, c=10.6897(5) Å, α=82.038(4)°, β=81.568(4)°, γ=76.938(4)°. CA-Pyz did not undergo a ferroelectric-type phase transition. Distortions occured in CA-Pyz crystal transforming the HT monoclinic structure (C2/m) to LT triclinic (P-1). We described the distortions in terms of rigid bodies and distortion-mode amplitudes. We found that the movements of chloranilic acid molecules appeared to be important at 235 K and the movements of pyrazine molecules appeared to be important at 275 K. Particularly, the distortion-mode amplitude r4 that are used to describe the rotation of pyrazine molecules drives the phase transition.

The crystal structure of 2-MBI was reinvestigated using variable temperature powder XRD, single crystal XRD and solid-state NMR. The crystal structure of 2-MBI appears unchanged between 120 K and 400 K. The LT structure was tetragonal, $P4_2/n$, with a=b=13.9506 (9) Å, c=7.1758 (7) Å, Z=1, R_w=9.790% initially determined by single crystal XRD. Due to the indication of crystal twinning, refinement using the monoclinic model (Pn) was attempted. Although a 90° rotation twin law was suggested, the reduction of R-factor was small. It appeared that the two component twinning model is insufficient.

Future works on chloranilic acid pyrazine will focus on more complex anisotropic peak shape model. In current work, a simple anisotropic peak shape model with only three coefficients (s040c, s400c and s220c) was used. We will investigate the distortions by refining all Stephen's peak shape coefficients and then fixing these values for all temperatures. In addition, the minimum and maximum limits of those coefficients need to be taken into account. Furthermore, the movements of chloranilic acid below 235 K and the movements of pyrazine below 275 K will be further studied.

Future research of 2-methylbenzimidazole is likely to focus on a low-temperature powder

X-ray diffraction. A recent work[85] revealed the pressure-induced ferroelectricity in 2-methylbenzimidazole. We probably need to carry out a powder X-ray diffraction at 12 K in order to investigate any potential structural phase transition.

References

1. S. Horiuchi and Y. Tokura, *Nat Mater*, 2008, **7**, 357-366.
2. S. Horiuchi, R. Kumai, J. Fujioka and Y. Tokura, *Physica B: Condensed Matter*, 2010, **405**, S334-S337.
3. S. Horiuchi, F. Kagawa, K. Hatahara, K. Kobayashi, R. Kumai, Y. Murakami and Y. Tokura, *Nat Commun*, 2012, **3**, 1308.
4. J. Li, Y. Liu, Y. Zhang, H.-L. Cai and R.-G. Xiong, *Physical Chemistry Chemical Physics*, 2013, **15**, 20786-20796.
5. A. S. Tayi, A. Kaeser, M. Matsumoto, T. Aida and S. I. Stupp, *Nat Chem*, 2015, **7**, 281-294.
6. I. Sumio, *Journal of Physics: Condensed Matter*, 2014, **26**, 493201.
7. S. Horiuchi, F. Ishii, R. Kumai, Y. Okimoto, H. Tachibana, N. Nagaosa and Y. Tokura, *Nat Mater*, 2005, **4**, 163-166.
8. Y. H. Roos and S. Drusch, in *Phase Transitions in Foods (Second Edition)*, Academic Press, San Diego, 2016, pp. 1-17.
9. J. Fousek, *Joseph Valasek and the discovery of ferroelectricity*, 1994.
10. J. Valasek, *Physical Review*, 1922, **19**, 478-491.
11. J. Valasek, *Physical Review*, 1921, **17**, 475-481.
12. C. A. Beevers and W. Hughes, *Proceedings of the Royal Society of London. Series A, Mathematical and Physical Sciences*, 1941, **177**, 251-259.
13. E. Suzuki and Y. Shiozaki, *Physical Review B*, 1996, **53**, 5217-5221.
14. X. Solans, C. Gonzalez-Silgo and C. Ruiz-Pérez, *Journal of Solid State Chemistry*, 1997, **131**, 350-357.
15. C. H. Gorbitz and E. Sagstuen, *Acta Crystallographica Section E*, 2008, **64**, m507-m508.
16. F. Mo, R. H. Mathiesen, J. A. Beukes and K. M. Vu, *IUCrJ*, 2015, **2**, 19-28.
17. F. Sandy and R. V. Jones, *Physical Review*, 1968, **168**, 481-493.
18. R. Blinc, V. Dimic, D. Kolar, G. Lahajnar, J. Stepišnik, S. Žumer, N. Vene and D. Hadži, *The Journal of Chemical Physics*, 1968, **49**, 4996-5000.
19. S. Koval, J. Kohanoff, J. Lasave, G. Colizzi and R. L. Migoni, *Physical Review B*, 2005, **71**, 184102.
20. W. Cai and A. Katrusiak, *Dalton Transactions*, 2013, **42**, 863-866.
21. J. C. Slater, *The Journal of Chemical Physics*, 1941, **9**, 16-33.
22. S. Koval, J. Kohanoff, R. L. Migoni and E. Tosatti, *Physical Review Letters*, 2002, **89**, 187602.
23. T. Fukami, *physica status solidi (a)*, 1990, **117**, K93-K96.
24. A. L. Solomon, *Physical Review*, 1956, **104**, 1191-1191.
25. G. J. Goldsmith and J. G. White, *The Journal of Chemical Physics*, 1959, **31**, 1175-1187.
26. H. Futama, *Journal of the Physical Society of Japan*, 1962, **17**, 434-441.
27. M. M. Elcombe and J. C. Taylor, *Acta Crystallographica Section A*, 1968, **24**, 410-420.
28. D. R. McKenzie and J. S. Dryden, *Journal of Physics C: Solid State Physics*, 1973, **6**, 767.
29. S. Tanisaki, H. Mashiyama and K. Hasebe, *Acta Crystallographica Section B*, 1988, **44**, 441-445.
30. I. Takahashi, A. Onodera and Y. Shiozaki, *Acta Crystallographica Section B*, 1990, **46**, 661-664.

31. M. Kroon, R. Kroon, R. Sprik and A. Lagendijk, *Journal of Applied Physics*, 1995, **77**, 806-810.
32. Y. Cai, S. Luo, Z. Zhu and H. Gu, *The Journal of Chemical Physics*, 2013, **139**, 044702.
33. S. Horiuchi, Y. Tokunaga, G. Giovannetti, S. Picozzi, H. Itoh, R. Shimano, R. Kumai and Y. Tokura, *Nature*, 2010, **463**, 789-792.
34. S. Horiuchi, R. Kumai and Y. Tokura, *Advanced Materials*, 2011, **23**, 2098-2103.
35. D. Di Sante, A. Stroppa and S. Picozzi, *Physical Chemistry Chemical Physics*, 2012, **14**, 14673-14681.
36. S. Mukhopadhyay, M. J. Gutmann, M. Jura, D. B. Jochym, M. Jimenez-Ruiz, S. Sturniolo, K. Refson and F. Fernandez-Alonso, *Chemical Physics*, 2013, **427**, 95-100.
37. M. Sikora, P. Pojawis and A. Katrusiak, *The Journal of Physical Chemistry C*, 2013, **117**, 14213-14217.
38. S. Horiuchi, R. Kumai, Y. Okimoto and Y. Tokura, *Chemical Physics*, 2006, **325**, 78-91.
39. G. Giovannetti, S. Kumar, A. Stroppa, J. van den Brink and S. Picozzi, *Physical Review Letters*, 2009, **103**, 266401.
40. H. Okamoto, T. Mitani, Y. Tokura, S. Koshihara, T. Komatsu, Y. Iwasa, T. Koda and G. Saito, *Physical Review B*, 1991, **43**, 8224-8232.
41. Y. Tokura, S. Koshihara, Y. Iwasa, H. Okamoto, T. Komatsu, T. Koda, N. Iwasawa and G. Saito, *Physical Review Letters*, 1989, **63**, 2405-2408.
42. A. Girlando, C. Pecile and J. B. Torrance, *Solid State Commun.*, 1985, **54**, 753-759.
43. E. Collet, M.-H. Lemée-Cailleau, M. Buron-Le Cointe, H. Cailleau, M. Wulff, T. Luty, S.-Y. Koshihara, M. Meyer, L. Toupet, P. Rabiller and S. Techert, *Science*, 2003, **300**, 612-615.
44. S. Horiuchi, Y. Okimoto, R. Kumai and Y. Tokura, *Science*, 2003, **299**, 229-232.
45. H.-Y. Ye, Y. Zhang, S.-i. Noro, K. Kubo, M. Yoshitake, Z.-Q. Liu, H.-L. Cai, D.-W. Fu, H. Yoshikawa, K. Awaga, R.-G. Xiong and T. Nakamura, *Scientific Reports*, 2013, **3**, 2249.
46. M. Le Cointe, M. H. Lemée-Cailleau, H. Cailleau, B. Toudic, L. Toupet, G. Heger, F. Moussa, P. Schweiss, K. H. Kraft and N. Karl, *Physical Review B*, 1995, **51**, 3374-3386.
47. K. Kobayashi, S. Horiuchi, R. Kumai, F. Kagawa, Y. Murakami and Y. Tokura, *Physical Review Letters*, 2012, **108**, 237601.
48. J. B. Torrance, *Phys. Rev. Lett.*, 1981, **47**, 1747-1750.
49. J. B. Torrance, J. E. Vazquez, J. J. Mayerle and V. Y. Lee, *Phys. Rev. Lett.*, 1981, **46**, 253-257.
50. P. Lunkenheimer and A. Loidl, *Journal of Physics: Condensed Matter*, 2015, **27**, 373001.
51. S. Horiuchi, R. Kumai and Y. Tokura, *Journal of Materials Chemistry*, 2009, **19**, 4421-4434.
52. S. Horiuchi, *Nature Mater.*, 2005, **4**, 163-166.
53. S. Horiuchi, R. Kumai and Y. Tokura, *Chemical Communications*, 2007, 2321-2329.
54. R. Kumai, S. Horiuchi, J. Fujioka and Y. Tokura, *Journal of the American Chemical Society*, 2012, **134**, 1036-1046.
55. S. Horiuchi, R. Kumai and Y. Tokura, *Angew. Chem. Int. Ed.*, 2007, **46**, 3497-3501.
56. R. Kumai, S. Horiuchi, Y. Okimoto and Y. Tokura, *J. Chem. Phys.*, 2006, **125**, 084715.
57. S. Horiuchi, R. Kumai and Y. Tokura, *Journal of the American Chemical Society*, 2013, **135**, 4492-4500.
58. T. Umanodan, S. i. Tanaka, S. Naruse, T. Ishikawa, K. Onda, S.-y. Koshihara, S. Horiuchi and Y. Okimoto, *Journal of the Physical Society of Japan*, 2015, **84**, 073707.
59. M. Ladd and R. Palmer, in *Structure Determination by X-ray Crystallography: Analysis by X-rays and Neutrons*, Springer US, Boston, MA, 2013, pp. 111-159.
60. K. D. M. Harris and P. A. Williams, in *Structure from Diffraction Methods*, John Wiley & Sons, Ltd, 2014, pp. 1-81.

61. L. Smart and E. A. Moore, *Solid state chemistry : an introduction*, 3rd ed. edn., CRC Press, Boca Raton, 2005.
62. B. Fultz and J. Howe, in *Transmission Electron Microscopy and Diffractometry of Materials*, Springer Berlin Heidelberg, Berlin, Heidelberg, 2013, pp. 1-57.
63. L. Smart and E. Moore, *Solid state chemistry : an introduction*, 4th ed. edn., CRC Press, Boca Raton, 2012.
64. C. Hammond and C. International Union of, *The basics of crystallography and diffraction*, 3rd ed. edn., Oxford University Press, Oxford ; New York, 2009.
65. A. R. West, *Basic solid state chemistry*, Second edition. edn., Wiley, Chichester, 1999.
66. A. C. Altomare, G.; Giacovazzo, C.; Guagliardi, A.; Burla, M.C.; Polidori, G.; Camalli, M, *Journal of Applied Crystallography*, 1994, **27**, 437.
67. P. W. Betteridge, Carruthers, J.R., Cooper, R.I., Prout, K., Watkin, D.J, *Journal of Applied Crystallography*, 2003, **36**, 1487.
68. J. R. Carruthers and D. J. Watkin, *Acta Crystallographica Section A*, 1979, **35**, 698-699.
69. R. A. Young, *Rietveld method*, New ed. edn., Oxford University Press, Oxford, 1995.
70. H. M. Rietveld, *Journal of Applied Crystallography*, 1969, **2**, 65-&.
71. A. A. Coelho, J. S. O. Evans, I. R. Evans, A. Kern and S. Parsons, *Powder Diffraction*, 2011, **26**, S22.
72. in *Powder Diffraction: The Rietveld Method and the Two Stage Method to Determine and Refine Crystal Structures from Powder Diffraction Data*, Springer Berlin Heidelberg, Berlin, Heidelberg, 2006, pp. 41-72.
73. L. B. McCusker, R. B. Von Dreele, D. E. Cox, D. Louer and P. Scardi, *Journal of Applied Crystallography*, 1999, **32**, 36-50.
74. C. Dybowski and S. Bai, *Analytical Chemistry*, 2006, **78**, 3853-3858.
75. S. Horiuchi, R. Kumai, Y. Tokunaga and Y. Tokura, *Journal of the American Chemical Society*, 2008, **130**, 13382-13391.
76. H. Ishida and S. Kashino, *Acta Crystallographica Section C*, 1999, **55**, 1923-1926.
77. H. Ishida and S. Kashino, *Acta Crystallographica Section C-Crystal Structure Communications*, 1999, **55**, 1923-1926.
78. B. J. Campbell, H. T. Stokes, D. E. Tanner and D. M. Hatch, *Journal of Applied Crystallography*, 2006, **39**, 607-614.
79. M. Muller, R. E. Dinnebier, A.-C. Dippel, H. T. Stokes and B. J. Campbell, *Journal of Applied Crystallography*, 2014, **47**, 532-538.
80. P. S. Costa, D. P. Miller, J. D. Teeter, S. Beniwal, E. Zurek, A. Sinitskii, J. Hooper and A. Enders, *The Journal of Physical Chemistry C*, 2016, **120**, 5804-5809.
81. J. Seliger and V. Žagar, *The Journal of Physical Chemistry C*, 2013, **117**, 20193-20200.
82. A. E. Obodovskaya, Z. A. Starikova, S. N. Belous and I. E. Pokrovskaya, *Journal of Structural Chemistry*, 1991, **32**, 421-422.
83. C. Bonhomme, C. Gervais, F. Babonneau, C. Coelho, F. Pourpoint, T. Azaïs, S. E. Ashbrook, J. M. Griffin, J. R. Yates, F. Mauri and C. J. Pickard, *Chemical Reviews*, 2012, **112**, 5733-5779.
84. S. J. Clark, M. D. Segall, C. J. Pickard, P. J. Hasnip, M. J. Probert, K. Refson and M. C. Payne, *Zeitschrift für Kristallographie*, 2005, **220**, 567-570.
85. W. Zieliński and A. Katrusiak, *Crystal Growth & Design*, 2014, **14**, 4247-4253.

Appendix 1 Courses and trainings

1. Material chemistry course
2. Powder diffraction and Rietveld refinement (PDRR) school 2016
3. ISIS Crystallography Users meeting 2015

Appendix 2 A list of Seminars

1. “Thin-Film Solar Cells”, Dr Budhika Mendis
2. “Cooperative Capture Rotaxane Synthesis”, Prof Sir Fraser Stoddart
3. “Serendipity at Work”, Prof Sir Fraser Stoddart
4. “The Nature of the Mechanical Bond: From Molecules to Machines”, Prof Sir Fraser Stoddart
5. “Mechanistic Insights into the Structure-Property Relationship through detailed Crystallographic Studies”, Dr Mark Senn
6. “Atomic-Scale Insights into Energy Materials (Batteries Included)”, Prof. Saiful Islam
7. "Recent Developments in Asymmetric Catalysis and Total Synthesis", Prof. Patrick Guiry
8. “Clean and efficient energy generation: Materials for solid oxide fuel cells”, Dr Ivana Evans
9. “Catalysis on Gold”, Professor Graham Hutchings FRS
10. “Mechanisms and inhibition of multidrug transporters in health and disease”, Dr Hendrik van Veen

Appendix 3 Summaries of two seminars

1. “Cooperative Capture Rotaxane Synthesis”， Prof Sir Fraser Stoddart

   In this talk, Prof Sir Fraser Stoddart introduced the synthesis of rotaxane and oligorotaxane followed by the applications of oligorotaxane. An extremely efficient way to produce a single rotaxane is to use the dumbbell as a template. Two imine bonds and hydrogen bonds were formed during the formation of the rotaxane. Then, he talked about the formation of [3]rotaxane and [4]rotation, as well as the synthesis of extended aldehydes. The proton NMR spectra were used to characterise the synthesised rotaxane and could provide the evidence for rigidity. He showed the

results of cooperativity in the [3]rotaxane and [4]rotaxane. [3]rotaxane did not exhibit any cooperativity operating. However, [4]rotaxane showed positive cooperativity operating. After that, he mentioned the formation of oligo[n]rotaxane and the comparison of each oligorataxane. Finally, he pointed out the applications of oligorotaxane. Oligorotaxanes are able to used in the fild of authentication and supramolecular encryption.

2. “Mechanistic Insights into the Structure-Property Relationship through detailed Crystallographic Studies”, Dr Mark Senn

   Dr Mark Senn talked about how investigate the structures of materials using an idea of phonon modes. He is interested in order-disorder phase transitions, where the local symmetry breaking is not the same as the global symmetry breaking, and hence a degree of disorder must exist. He illustrated perovskite $BaTiO_3$ which exhibits room temperature ferroelectricity as an example. He has been studied this system, gaining new insight into how global and local symmetry breaking can be reconciled with each other. At high temperature, it possesses a mirror plane and the dipole moments cancel out each other. Thus, the molecule is in its disordered phase. At low temperature, symmetry breaking occurs. Distortion removes the mirror plane and the molecule is in its ferroelectric phase. Senn described the distortion appearing in $BaTiO_3$ in terms of phonon modes. When the molecule is in its ferroelectric phase, the phonon modes go “soft” and require zero energy. A term “frozen phonon” referred to the situation when symmetry adapted distortion. If a structure and its distorted structure show group-subgroup relationship, it always can use phonon modes to describe the phase transition. Furthermore, he talked about how properties can be influenced by distortions. Negative thermal expansion is one of the properties he discussed that is caused by symmetry distortions, where phonon modes become zero at high temperature.